



HAL
open science

Phenotyping Polarization Dynamics Of Immune Cells Using A Lipid Droplet - Cell Pairing Microfluidic Platform

Léa Pinon, Nicolas Ruysen, Judith Pineau, Olivier Mesdjian, Damien Cuvelier, Anna Chipont, Rachele Allena, Coralie L Guerin, Sophie Asnacios, Atef Asnacios, et al.

► **To cite this version:**

Léa Pinon, Nicolas Ruysen, Judith Pineau, Olivier Mesdjian, Damien Cuvelier, et al.. Phenotyping Polarization Dynamics Of Immune Cells Using A Lipid Droplet - Cell Pairing Microfluidic Platform. 2022. hal-03853948v1

HAL Id: hal-03853948

<https://hal.science/hal-03853948v1>

Preprint submitted on 15 Nov 2022 (v1), last revised 15 Nov 2022 (v2)

HAL is a multi-disciplinary open access archive for the deposit and dissemination of scientific research documents, whether they are published or not. The documents may come from teaching and research institutions in France or abroad, or from public or private research centers.

L'archive ouverte pluridisciplinaire **HAL**, est destinée au dépôt et à la diffusion de documents scientifiques de niveau recherche, publiés ou non, émanant des établissements d'enseignement et de recherche français ou étrangers, des laboratoires publics ou privés.

Phenotyping Polarization Dynamics Of Immune Cells Using A Lipid Droplet - Cell Pairing Microfluidic Platform

Léa Pinon^{1,2,3}, Nicolas Ruysen⁴, Judith Pineau², Olivier Mesdjian^{1,3}, Damien Cuvelier^{3,5,11}, Anna Chipont⁶, Rachele Allena^{4,8}, Coralie L. Guerin^{6,7}, Sophie Asnacios^{9,10}, Atef Asnacios⁹, Paolo Pierobon^{2,11}, and Jacques Fattaccioli^{1,3,11}

¹École Normale Supérieure, UMR 8640, Laboratoire P.A.S.T.E.U.R., Département de Chimie, PSL Research University, Sorbonne Université, CNRS, 75005 Paris, France

²Institut Curie, U932, Immunology and Cancer, INSERM, 75005 Paris, France

³Institut Pierre-Gilles de Gennes pour la Microfluidique, 75005 Paris, France

⁴Arts et Métiers Institute of Technology, Université Paris 13, Sorbonne Paris Cité, IBHGC, HESAM Université, F-75013 Paris, France

⁵Institut Curie, UMR 144, PSL Research University, CNRS, Paris, France

⁶Institut Curie, Cytometry Platform, F-75005, Paris, France.

⁷Université Paris Cité, INSERM, Innovative Therapies in Haemostasis, F-75006, Paris, France.

⁸LJAD, UMR 7351, Université Côte d'Azur, 06100, Nice, France

⁹Université de Paris, CNRS, Laboratoire Matière et Systèmes Complexes, UMR 7057, F-75013, Paris, France

¹⁰Sorbonne Université, Faculté des Sciences et Ingénierie, UFR 925 Physics, F-75005 Paris, France

¹¹Sorbonne Université, Faculté des Sciences et Ingénierie, UFR 926 Chemistry, F-75005 Paris, France

Abstract

The immune synapse is the tight contact zone between a lymphocyte and a cell presenting its cognate antigen. This structure serves as a signaling platform and entails a polarization of intra-cellular components, necessary to the immunological function of the cell. While the surface properties of the presenting cell are known to control the formation of the synapse, their impact on polarization has not yet been studied.

Using functional lipid droplets as tunable artificial presenting cells combined with a microfluidic pairing device, we simultaneously observe synchronized synapses and dynamically quantify polarization patterns of individual B cells. By assessing how ligand concentration, surface fluidity and substrate rigidity impact lysosome polarization, we show that its onset and kinetics depend on the local antigen concentration at the synapse and on substrate rigidity. Our experimental system enables a fine phenotyping of monoclonal cell populations based on their synaptic readout.

Oil-in-water droplets| B cell synapse| microfluidics| cell polarity| mechanosensitivity

Correspondence: paolo.pierobon@curie.fr and jacques.fattaccioli@ens.psl.eu

Introduction

Direct contact is an important channel of communication for cells in multicellular organisms. This is true for cells in tissues as well as for cells that mostly live as independent entities like immune cells (1). Their activation, their immune function and ultimately their fate depend on signal exchanges with other cells through an organized structure called immune synapse. In both B and T lymphocytes, the formation of the immune synapse is associated with a global rearrangement of the cytoskeleton and the establishment of a polarity axis (2–4). B lymphocytes, the cells responsible for antibody production, encounter antigens in the subcapsular sinus of the lymph node, in soluble form or grafted on other cell surface such as macrophages or follicular dendritic cells. They recognize the antigen through their specific B cell receptor (BCR), internalize, process and further present it to a cognate T cell. Antigen recognition entails membrane and intracellular reorganizations leading to the formation of the immune synapse (5). Engagement of the BCR leads to the clusterization of signaling complexes in a mechanosensitive way: signaling and size of the complexes depend on the rigidity and topography of the substrate (6–8). The synapse, in its final form, displays a stereotypical concentric shape with antigens/BCRs

25 accumulated in a central cluster, surrounded by adhesion molecules and an actin ring at the periphery (9–11). A similar
26 geometry is mirrored by cytoplasmic molecules close to the membrane (12). At the same time, the microtubule network
27 re-orientes the traffic towards the synapse (polarization of the centrosome) to secrete lysosomal proteases and degrade
28 the antigen in the synaptic cleft, in a process named enzymatic extraction (13). It has been shown that, depending on
29 the deformability of the substrate, the antigen can be internalized also by mechanical pulling (14–17). When mechanical
30 extraction fails, such as on non-deformable substrates, cells trigger the enzymatic extraction pathways described above
31 (15). Interestingly, the mutual exclusivity of mechanical and enzymatic extractions suggests that the polarization mech-
32 anism is also sensitive to the mechanical properties of the substrate. Ultimately, the B cell immune synapse results in
33 signal transduction, cell differentiation and production of high-affinity antibodies (2). It has been also proposed that by
34 polarizing, B cells can divide asymmetrically to give rise to B cells that present more efficiently the antigen to T cells.
35 Polarity, therefore, has consequences on B cell fate (18, 19).

36 All these experimental results point to a crucial role of physico-chemical properties of the antigen presenting surface in
37 B cell activation. Different systems have been used to address this mechanism. For instance, clusters formation has
38 been revealed on fluid interfaces allowing antigen mobility (lipid bilayers (9)); mechanosensitivity has been shown using
39 deformable substrates such as soft gels (6, 7); antigen mechanical extraction has been uncovered on plasma membrane
40 sheets (14), and quantified by calibrated DNA force sensors (15, 20). Despite the amount of information gathered in these
41 systems, the variety of assays hinders the comparison between experiments performed on different materials and makes
42 it impossible to evaluate the impact of independent properties on the synapse formation. This prompts us to introduce a
43 new model to stimulate B cells while independently controlling physical (rigidity, fluidity, size) and chemical (functionaliza-
44 tion) properties: lipid droplets.

45 Emulsions are colloidal liquid-liquid metastable suspensions stabilized by a surfactant monolayer, that have already shown
46 their biocompatibility and their interest as probes when functionalized with proteins of interests in biophysical (21), devel-
47 opmental (22), and immunological contexts such as phagocytosis (23–25) or T cell synapse studies (26). By varying the
48 bulk and surface composition, it is possible to tune the surface tension, hence the mechanical rigidity, independently from
49 the ligand surface concentration, thus making lipid droplets a relevant antigen-presenting cell (APC) surrogate to stimulate
50 B cells with the highest control on the physico-chemical properties of the cognate surface.

51 In this work, we introduce new droplet formulations and functionalization to access different physical and chemical prop-
52 erties that we finely characterize. Finally, we validate our methods n addressing how cells polarize depending on the
53 properties of those antigen-presenting substrates. This question has been neglected in the past, partially because of
54 the heterogeneity of experimental models, partially because of the lack of reproducible way to study the global cell re-
55 arrangement following immune synapse formation over time. Therefore, for a proper quantitative study, we engineered
56 antigen-functionalized lipid droplets with a pertinent set of physico-chemical properties and presented them to B cells in
57 a controlled microfluidic pairing device that minimizes the stress to mimic the flow conditions of the lymph node. This
58 allowed us to simultaneously observe multiple synchronized synapses with a high spatio-temporal resolution and finally
59 provide a phenotyping map of variability of B cell polarity both in terms of polarization onset and kinetics.

60 Results

61 Microfluidic cell-cell pairing platform for the study of B cell synapses

62 To characterize the influence of rigidity and antigen concentration on B cell polarity, we observe by epifluorescence
63 microscopy the polarization of murine B cells activated by antigen-coated fluid microparticles having different mechanical
64 and interfacial properties.

65 Because B cells are non-adherent cells, to control in space and time B cell synapse, we used a microfluidic chip that forces
66 the encounter between a single B cell and an activating APC surrogate (**Fig. 1A**). The microfluidic chip (**Fig. 1B**), inspired
67 by (27), consists of staggered arrays of double-layered U-shaped traps where the two objects (ideally of the same size)
68 are sequentially immobilized (**Supplementary Note 1**) and imaged. The double layer structures result in fluid streamlines
69 not being deviated from the weir structures when a first object is trapped, thus allowing the easy capture of a second
70 object (27, 28). The trapping array was engineered to apply the least perturbative shear stress as possible on the cells,
71 mimicking the *in vivo*-like shear stress estimated in the subcapsular sinus lumen of lymphoid tissues (29). Finite element
72 simulations (**Supplementary Note 1**) indicate that, at the inlet speed used in our experiments, the maximal wall shear
73 stresses on wall (**Fig. 1C**) and trapped cell (**Fig. 1D**) are below 1 Pa (value compatible with the shear stress estimated
74 in the lymph node (29)). Overall, the microfluidic chip we designed minimizes the stress to mimic conditions that a cell
75 experiences in lymph nodes.

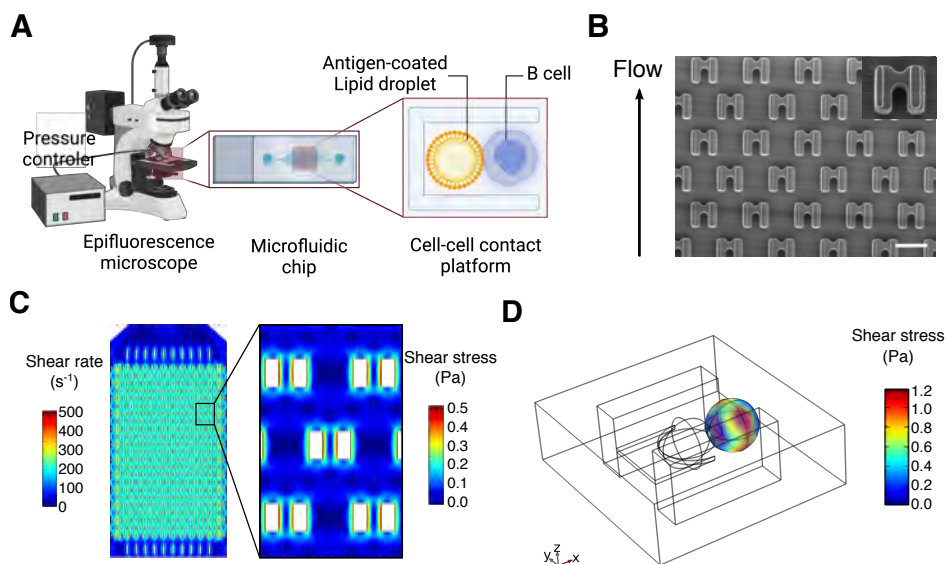


Fig. 1. Microfluidic cell-cell pairing platform for the study of B cell synapses. (A) Schematic view of the experimental setup. The microfluidic trap-based chip is imaged with an epifluorescence video-microscope, and is connected to a pressure controller inducing a low flow for droplets - then cells - circulation. (B) SEM images of the microfluidic chamber containing 288 two-layered traps. Scale bar: 30 μm. (C) 2D FEM simulation of fluid shear rate (left) and shear stress (right) passing through the pillars along the whole chip, for an inlet pressure of 1000 Pa corresponding to a maximal fluid velocity of 1.6 mm/s. The shear rate is constant along the chamber. The maximal wall shear rate is about 514 s⁻¹ that corresponds to a maximal wall shear stress about 0.514 Pa. (D) 3D simulation of the shear stress that a trapped cell experiences in the microfluidic device when it is immobilized with a droplet (wireframe representation). For a maximal inlet pressure of 1000 Pa - maximal fluid velocity of 1.6 mm/s in the chamber - the maximal shear stress is about 1.0 Pa.

76 Droplets mimic APC both in antigen concentrations and mechanical properties

77 Our study has been conducted with B lymphoma murine cell line IIA1.6, which is described to be a homogeneous popu-
78 lation of non-activated mature B cells. These cells constitute an ideal model for functional studies of antigen presentation,
79 since they lack Fc γ RIIB1 receptors on their surface (30, 31) and hence can be conveniently activated through specific
80 antibodies against the BCR (F(ab')₂). We stimulated these cells with lipid droplets functionalized with such antibodies
81 (which will be referred to as antigens, Ag), linked to droplet surface with biotinylated phospholipids (DPSE-PEG₂₀₀₀-
82 Biotin)/streptavidin complex **Fig. 2A**. As negative control, droplets were coated with biotinylated BSA which do not engage
83 the BCR, in lieu of F(ab')₂ (17). In both cases, fluorescent streptavidin linker allows to observe the functionalization (**Fig.**
84 **2B**).

85 Lipid droplets were fabricated by shearing an oil phase in an aqueous buffer containing surface active agents (surfactants)
86 to improve suspension stability over time (32). To avoid a possible bias in the analysis of the synapse formation and cell
87 polarization, that could exist if cells were put into contact with particles of different diameters (hence curvature), we
88 decided to work with monodisperse size distributions with an average diameter of 11 μm , comparable to the one of a B
89 cell (**Fig. 2B-C**).

90 After droplet emulsification, we coated the droplet surface by adsorbing phospholipids onto the surface with the help of
91 a polar co-solvent, as done in (33). Then, fluorescent streptavidins, used as linker, was added to attach on the one side
92 to the biotinylated phospholipids, and bind to the other side to biotinylated F(ab')₂, added in the last step. This protocol
93 ensures a finely-controlled and homogeneous lipid coating. Ultimately, protein functionalization of the droplets surface
94 (streptavidin) is performed, as shown in **Fig. 2B** and **C**. To quantify the surface concentration in F(ab')₂, we used specific
95 and fluorescent secondary antibodies at saturating concentrations and correlated streptavidin fluorescence intensity to
96 assess the absolute F(ab')₂ concentration over droplet surface (**Supplementary Note 2**). **Fig. 2D** shows that the F(ab')₂
97 adsorption is well described by a Langmuir isotherm, making straightforward the quantification of their surface density
98 (**Supplementary Note 2**). F(ab')₂ surface density, expressed as a number of proteins per unit of surface area, has a
99 maximal value of 150 antigens/ μm^2 at saturating conditions. This value has been previously shown to be sufficient to
100 trigger B cell activation (10).

101 Antigen-presenting cells stiffness has been reported to be a relevant mechanical property for immune cell activation
102 (34, 35) and in particular for B cell functions (6, 15). The stiffness of a material is related to its ability to resist reversible
103 deformations when submitted to stress, i.e. to its apparent elastic properties. For oil droplets, the origin of elastic-like
104 resistance to deformation is expected to be the excess pressure inside the droplet, i.e. the Laplace pressure ΔP written
105 as $\Delta P = 2\gamma/R$, where R is the droplet radius. The stiffness of a droplet can, therefore, be modulated by changing the
106 surface tension γ between the oil and the surrounding liquid medium. We measured the surface tension of diverse droplet
107 formulations by the pendant drop technique and micropipette (36, 37) (**Fig. S1**). We found that the interfacial tension
108 of the oil/water interface ranges from about 1 to 12 mN/m between the softest and stiffest formulations, thus varying by
109 about one order of magnitude (**Fig. 2E**). In addition, micropipette aspiration (38) measurements on single functionalized

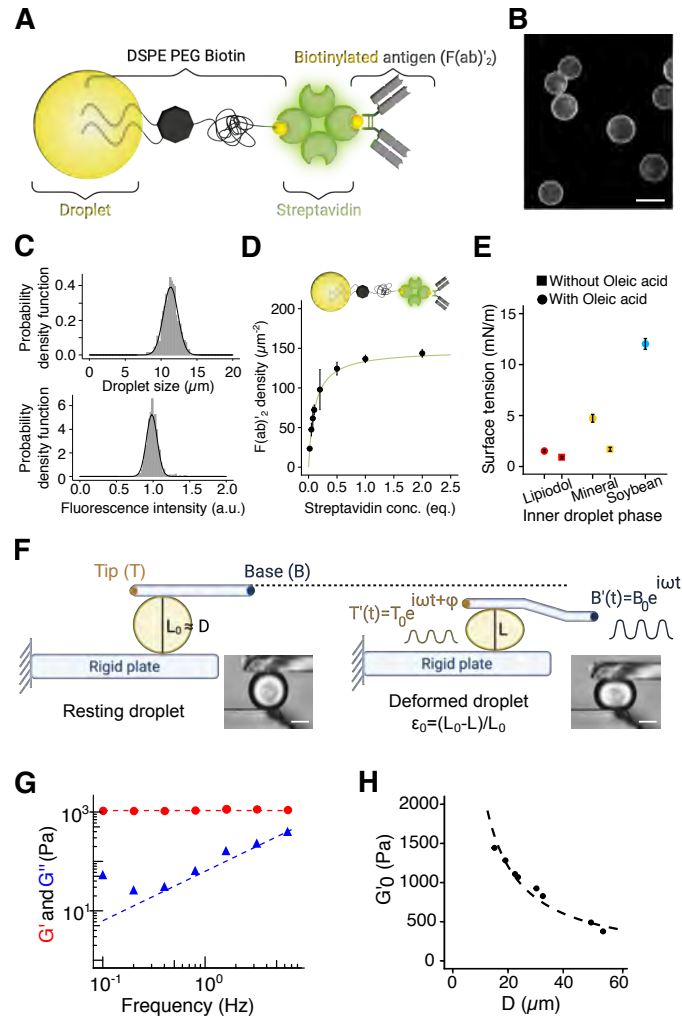


Fig. 2. Droplets mimic APC both in antigen concentrations and mechanical properties. (A) Schematic of the droplet coating complex with DSPE-PEG₂₀₀₀-Biotin / Streptavidin / F(ab)₂. (B) Representative epifluorescence image of coated droplet. Scale bar: 7 μm . (C) Size (mean \pm std = $11.0 \pm 0.7 \mu\text{m}$) and fluorescence (mean \pm std = 1 ± 0.075) histograms of $N = 700$ droplets. (D) Titration curve of F(ab)₂ fragments depending on the streptavidin concentration on droplets. The fit follows to the Langmuir's isotherm with a plateau at $147 \text{ F(ab)}_2/\mu\text{m}^{-2}$. These data are obtained from previous fluorescence intensity assessments of both streptavidin and F(ab)₂ on $11 \mu\text{m}$ -large droplets, initially functionalized with 100 equivalents of DSPE-PEG₂₀₀₀-biotin. (E) Pendant drop measurements of surface tension for three different oil mixtures - lipiodol (red), mineral (yellow) and soybean (blue) oils, enriched (dots) or not (squares) with oleic acid. (F) Schematic of the microplate experiment. A cell or a droplet is trapped between two glass microplates, one being immobile (bottom) the other flexible (top) with a base position oscillating as $B(t) = B_0 e^{i\omega t}$. We measure the oscillating displacement of the tip of the flexible plate as $T(t) = T_0 e^{i(\omega t + \phi)}$ that relates to the immobilized cell or droplet visco-elastic properties. T is determined for a frequency range between 0.1 Hz and 6.4 Hz (droplet) or 1.6 Hz (cells). Representative brightfield images of a resting (left) and a deformed (right) droplet. Scale bars: 30 μm . (G) Elastic G' and viscous G'' moduli of a single droplet (diameter: 19.1 μm) as a function of the probing frequency. In this frequency range, G' is constant, whereas G'' linearly depends on frequency. (H) Elastic modulus of droplets plotted as a function of the resting droplet diameter, for a constant initial deformation $\epsilon_0 = 0.2$. The fitting equation is written as $G' = 4\gamma/\epsilon L_0$ and leads to a surface tension $\gamma = 1.21 \pm 0.04 \text{ mN}\cdot\text{m}^{-1}$.

110 or non-functionalized droplets show that the effect of the phospholipids adsorption at the oil/water interfacial is negligible
111 (**Tables S2 and S3**).

112 The mechanical properties of complex materials are characterized by both an elastic and viscous behaviors (39) that
113 depends on the timescale of the solicitation. We used a microplate rheometer to measure the complex dynamic modulus
114 $G^*(f) = G' + iG''$ of single droplets over a frequency range of biological relevance (40), and to correlate the droplet
115 interfacial tension γ to their storage modulus G' (34, 41) (**Fig. 2F**).

116 The experiment consists in trapping a spherical deformable object between two glass microplates, a rigid and a flexible
117 one, and applying a sinusoidal deformation while measuring the resulting amplitude and phase shift at the tip of the
118 flexible microplate. From the applied oscillatory normal stress and the sinusoidal strain (deformation) of the object,
119 one can infer its complex dynamic modulus $G^*(f) = G' + iG''$, with the real part G' representing the storage modulus
120 (elastic-like response), and the imaginary part G'' accounting for energy dissipation (viscous-like response).

121
122 Sinking droplets (Lipiodol, oil denser than water, used here as reference) exhibited a Kelvin-Voigt behavior, with a constant
123 elastic modulus G' , and a viscous modulus G'' proportional to the frequency (**Fig. 2G**) where elastic-like response is
124 dominant ($G' \gg G''$, **Supplementary Note 3**). We found that, for a fixed strain ($\epsilon = 0.2$), the droplet storage modulus
125 decreases as the inverse of the diameter of the resting droplet (**Fig. 2H**), in agreement with the assumption that the only
126 restoring force resisting compression originates from Laplace pressure $\Delta P = 4\gamma/L_0$ (**Supplementary Note 3**), with L_0 the
127 resting droplet diameter. Thus, by fitting the storage modulus G' as function of the droplet diameter, one gets a calibration
128 curve for which we extract an estimation of the droplet surface tension, compatible with the pendant drop measurements
129 ($\gamma = 1.21 \pm 0.04$ mN/m - **Supplementary Note 3, Fig. 2E, Table S1-S2**). Therefore, according to this quantification,
130 we conclude that the droplets used in our experiments, i.e. diameter of 11 μm and tension ranging from 1 to 12 mN/m,
131 exhibit an apparent rigidity (storage modulus G') ranging from 4 to 30 kPa. As comparison, we used the same method to
132 measure B cell stiffness and found $G^* = 165$ Pa (**Supplementary Note 4 and Fig. S5**). Antigen presenting cells range
133 from 1 kPa (macrophages (34)) to 5-10 kPa (follicular dendritic cells (15), that are essentially fibroblasts). This indicates
134 that the droplets are, as APCs, several times stiffer than B cells and definitely in the range of the substrate rigidity capable
135 of eliciting a strong B cell signal according to (6).

136 **B cells actively gather antigens at the synapse**

137 We assessed the impact of antigen enrichment during the synapse formation by using two droplet types, one favoring
138 and the other one hindering such enrichment. We thus used two alternative methods to graft the lipids on the droplets:
139 via the surface where lipids are inserted after the emulsification processes (33), or in bulk where lipids are inserted prior
140 to emulsification (23, 26). Using the microfluidics traps described above to immobilize the droplet-B cell contact, we
141 notice that cells interacting with bulk-functionalized droplets gather the antigen to a sustainable central cluster (**Fig. 3A**,
142 **Movie S1**) in less than 20 min, similarly to what described on planar lipid bilayers (10) or for other cell types (23). By
143 contrast, surface-functionalized droplets do not allow antigen accumulation (**Fig. 3B**), similar to the negative BSA control

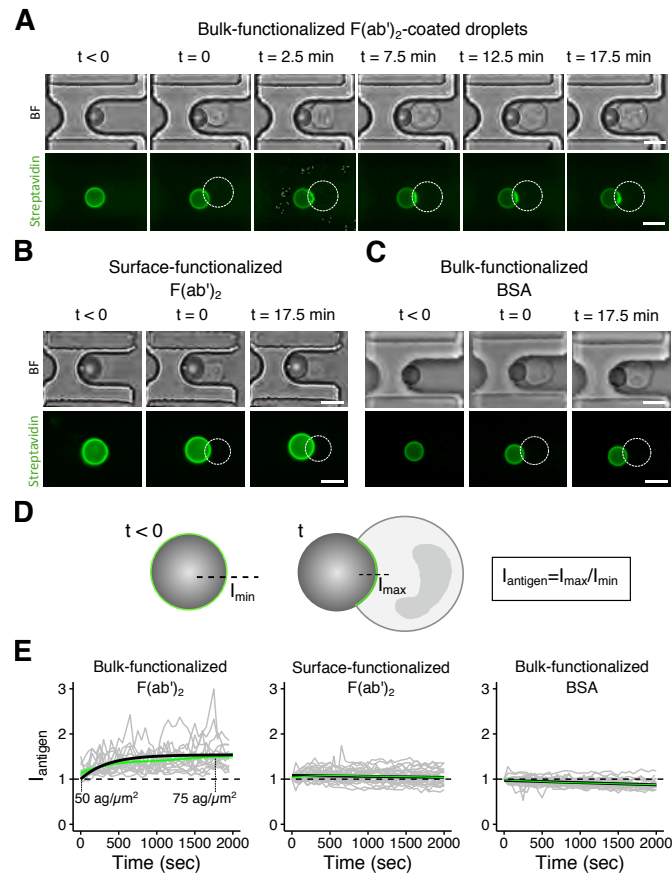


Fig. 3. B cells actively gather antigens at the synapse. (A) Time lapse images of the antigen aggregation in a bulk-functionalized droplet-cell contact. All droplets are functionalized with 50 $F(ab)_2$ fragments/ μm^2 on average. Scale bar: 10 μm . (B) Time lapse images of the antigen aggregation (not occurring) in a surface-functionalized droplet-cell contact. Droplets are functionalized with 100 $F(ab)_2$ fragments/ μm^2 . Scale bar: 10 μm . (C) Time lapse images of the antigen aggregation in a BSA bulk-functionalized droplet-cell contact. Droplets are functionalized with 100 BSA/ μm^2 . Scale bar: 10 μm . (D) Scheme of antigen accumulation analysis. The antigen recruitment index ($I_{antigen}$) is defined as the ratio of the intensity at the time zero (I_{min}) and the intensity over time (I_{max}), both at the synapse area. (E) $I_{antigen}$ time evolution for three different conditions. Only bulk-functionalized antigen-coated droplets show antigen recruitment (left, N=18 cells), while neither bulk-functionalized BSA-coated (right, N=27 cells) nor surface-functionalized antigen-coated droplets (center, N=34 cells) show antigen accumulation. For the bulk-functionalized antigen-coated droplets, the kinetic of antigen accumulation follows $y = (p - 1)(1 - \exp(-t/\tau)) + 1$, where $\tau = 5.07 \pm 0.14$ s. The related plateau $p = 1.50 \pm 0.06$ allow to calculate the number of antigens aggregated at the synapse by the cell: drop lets are initially coated with 50 antigens per μm^2 and cells cluster up to $1.5 \times 50 = 75$ antigens/ μm^2 . Green solid curves represent average values of all cells at each time point, and shaded surrounded curves the related 95% confidence interval.

144 **(Fig. 3C)**. We further quantified the kinetics of antigen accumulation by an index $I_{antigen}$ (**Fig. 3D**) that increases for
145 bulk-functionalized antigen-coated droplets as a monotonic exponential saturation curve over 40 min, with a characteristic
146 time of 5 min (**Fig. 3E**, bulk-functionalized antigen-coated droplets). The plateau is directly related to the accumulated
147 antigen concentration: the cluster is 1.5-fold brighter than the initial time point (**Fig. 3E**). We took advantage of the fine
148 calibration of antigen concentration showed above (**Fig. 2E and Supplementary Note 2**) to conclude that B cells are
149 able to gather up to 75 antigens/ μm^2 on droplets in 15 min (plateau, **Fig. 3E**) functionalized with initially 50 antigens/ μm^2
150 (Antigen^{low}) (time zero, **Fig. 3E**). We thus named the two types of functionalization - favoring and hindering antigen
151 gathering - respectively cluster⁺ and cluster⁻. We will further inquire whether antigen accumulation is an important
152 feature impacting the polarization of B cells.

153 **B cells exhibit different polarization responses after being activated**

154 As a proxy for cell polarization, we followed lysosomes distribution in time - as it has been already intensively studied as a
155 polarization readout (12, 13, 15, 42) - by imaging them using an acidic compartment dye (LysoTracker®) over 40 min. This
156 method is fast, reliable and does not interfere with organelles and cytoskeleton dynamics (13). We observe three distinct
157 behaviors for B cells even in contact with the same droplet type (**Fig. 4A**): within 40 min from the contact, lysosomes either
158 stay uniformly distributed in the cytoplasm (*no polarization*), move toward the synapse area (*polarization*, **Movie S2**), or
159 accumulate in the side opposite to synapse (*anti-polarization*, **Movie S3**). We quantified the asymmetry in lysosomes
160 distribution (polarity) by defining a polarization index I_{pol} as the ratio between the fluorescence signals in the half cell
161 close and opposite to the droplet, as sketched in **Figure 4B**.

162 We investigated the impact of antigen enrichment, antigen concentration and droplet stiffness on lysosome polariza-
163 tion. We compared the cellular responses upon interaction with five different droplets: stiffness^{low} ($\gamma = 1.7$ mN/m),
164 stiffness^{medium} ($\gamma = 4.7$ mN/m) or stiffness^{high} ($\gamma = 12$ mN/m), covered with 50 (Antigen^{low}) or 100 (Antigen^{high})
165 antigen/ μm^2 , with bulk- (cluster⁺) or surface-functionalized (cluster⁻) droplets (**Fig. 4C and 4D**). The panel of activat-
166 ing droplets allows to investigate the effect on polarization of different stiffness (at constant antigen concentration) and
167 different antigen coating conditions (at constant stiffness).

168 To establish the value of I_{pol} for which we consider a cell to be polarized or not, we observe the I_{pol} distribution for cells in
169 contact with the non-activating droplet (BSA-coated, gray plot **Fig. 4C**). As spontaneous polarization has been reported
170 (43), we considered two sigmas of the I_{pol} distribution for BSA-coated droplets as a threshold. This results in classifying
171 the cells with $I_{pol} \geq 1 + 2\sigma = 1.18$ as polarized. Symmetrically, we defined cells with $I_{pol} < 1 - 2\sigma = 0.82$ as anti-polarized
172 and, consequently, $0.82 \leq I_{pol} < 1.18$ for non-polarized cells (**Fig. 4C**). Furthermore, to check that the polarization occurs
173 specifically upon BCR engagement, we performed two major controls: (i) we excluded an impact of the flow by checking
174 that no cell polarized in absence of interaction at maximal flow of 1.6 mm/s (Control #1, **Fig. S2**); (ii) we excluded an
175 activation from potential soluble antigens coming from the droplet functionalization by observing no polarized cells among
176 the non-interacting ones in the presence of antigens-coated droplet in nearby traps (Control #2, **Fig. S2**). Altogether,
177 these results show that B cells polarize only when they form a specific contact with antigen coated-droplets suggesting

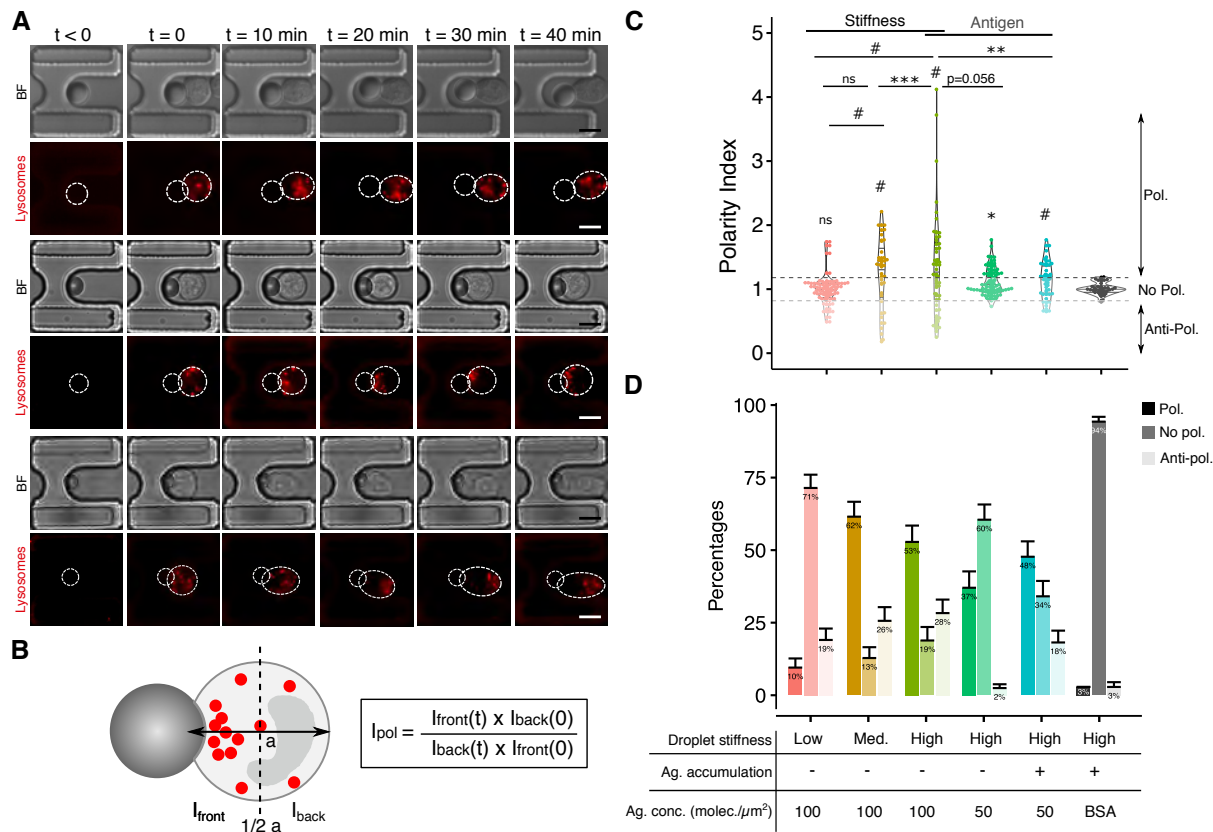


Fig. 4. B cells exhibit different polarization responses after being activated, and the onset of polarity is determined by stiffness and local concentration at the synapse. (A) Representative time-lapse imaging of the three cell behaviors: non-polarizing (top, droplet: 4 kPa - cluster⁻ - 100 ag/ μm^2 , $I_{pol} = 0.92$), polarizing (center, droplet: 29.8 kPa - cluster⁺ - 50 ag/ μm^2 , $I_{pol} = 1.21$), and anti-polarizing (bottom, droplet: 29.8 kPa - cluster⁻ - 100 ag/ μm^2 - $I_{pol} = 0.34$) cells. Scale bar: 10 μm . (B) Schematic representation of the polarization analysis and quantification: the polarization index (I_{pol}) is the ratio between the fluorescence intensity integrated over the front part, in contact with the droplet, and the fluorescence intensity integrated over the back of the cell. The ratio is normalized by its value at time zero. (C) Distribution of the I_{pol} , p -values are computed by pairwise Kolmogorov-Smirnov test — when not written, the pair is not significantly different. I_{pol} is the value for which the polarization behavior is sustained, i.e. at 40 min. (D) Percentages of the three cell behaviors depending on the droplet types, error bars are computed as half standard deviation of the percentage obtained by random subsampling 1000 groups of 15 values (typical size of the experimental pool in one day). Stiffness^{low}, Stiffness^{medium} and Stiffness^{high} in the text, denotes quantitative stiffness of respectively 4.0, 11.7 and 29.8 kPa. Antigen concentration relative to 100 and 50 antigens/ μm^2 denotes respectively Antigen^{high} and Antigen^{low}. Respective number of analyzed cells from left (pink plot) to right (gray plot): N=50, N=39, N=53, N=85, N=56, N=34, from at least 3 independent experiments. p -values: # : $p < 0.0001$, *** $p < 0.001$, ** $p < 0.01$, * $p < 0.05$.

178 that polarization is triggered by specific BCR engagement in our system, and that flow conditions do not alter polarization
179 in our experiments.

180 **Figure 4C** shows the polarity index distributions of the global cell populations for each droplet condition. For more accurate
181 analysis in each cell population, we classified the cells in the three categories of phenotypes described above (**Fig. 4D**).

182 B cell polarization onset depends on antigen concentration and droplet stiffness

183 We first studied the mechanosensitivity of the polarization process by changing the surface tension of the droplets, hence
184 their effective stiffness. For soft droplets, cells behave essentially as the negative control, although antipolarized cell
185 number increases. However, increasing stiffness from 4 kPa to 11.7 kPa, induces a greater number of polarized cells
186 and with much higher indexes, corresponding to an increased lysosome concentration in the synaptic area. Polarity
187 indexes distributions do not significantly change between stiffness^{medium} (4 kPa) and stiffness^{high} (≈ 12 kPa). These
188 results show that polarization is a mechanosensitive process and that the threshold of effective stiffness triggering the
189 polarization is between 4 and 12 kPa. Of note, antigen concentration does not depend on droplet stiffness (**Fig. S6**)

190 The major difference between bulk and surface functionalized droplets, antigen gathering, is related to the different fluidity
191 of the surfaces, as we showed by FRAP experiments (**Supplementary Note 5** and **Fig. S7**). Of note, surface tension does
192 not depend on functionalization method (**Fig. S8**). We characterized, therefore, the effects of both antigen concentration
193 and gathering on B cell polarization, by using droplets of similar stiffness (high). Surprisingly, despite not showing antigen
194 accumulation (**Fig. 3B**), cluster⁻ droplets stimulate rather well B cell polarization regardless of antigen concentration. Re-
195 markably, cluster⁺/Antigen^{low} droplets, inducing antigen enrichment, are able to generate the same amount of polarized
196 cells (52%) as cluster⁻/Antigen^{high} (55%) conditions which initially bear twice as much antigens (respectively 50 and
197 100 antigens/ μm^2). However, even in polarized cells, polarity indexes are lower in cluster⁺ cells, suggesting that a higher
198 local concentration of antigen stimulates stronger lysosome polarization. In addition, on cluster⁻ droplets, when antigen
199 concentration is halved, the percentage of polarized cells decreases from 55% to 35% (**Fig. 4D**). These results show that
200 by increasing local concentration at the synapse, antigen accumulation overcomes the lack of initial presented antigens
201 and lowers the threshold to established polarity when the density of presented antigens is below 75 antigens/ μm^2 .

202 A recapitulation of all conditions and outcome of polarization is shown in **Table 1**. **Figure 4D** shows that the population
203 of antipolarized cells does not change with stiffness for droplets cluster⁻ coated with a high concentration of ligands,
204 suggesting that for such interfacial conditions, antipolarization does not depend on the mechanics of the lipid droplet.
205 Considering the set of stiff droplets with contrasting interfacial properties, our result show that cluster⁺ droplets with a low
206 ligand level share a similar antipolarization value than cluster⁺ droplets with a high ligand level. On the contrary to the
207 polarization measurement, antipolarization fully disappears for cluster⁻ droplets coated with a low amount of antigens.
208 Although origin of such discrepancy remains elusive, these results suggest that polarization and antipolarization behaviors
209 come from two distinct mechanisms.

210 **The polarization kinetic is affected by droplet mechanical properties**

211 We then assessed the impact of droplet properties on the B cell polarization dynamics by measuring the evolution of the
212 polarization index I_{pol} over time (**Fig. 5 A-C**, **Fig. S9** and **Fig. S10**). The kinetics of *polarization (anti-polarization)* events
213 shows increasing (decreasing) curves that reach a steady state about 15 min after the droplet-cell encounter. Lysosomes
214 polarity depends on microtubule network orientation and organelles motility on this network. One single parameter cannot
215 capture this complex kinetics. We chose the model that appears to us by visual inspection of the kinetic curves: an
216 exponential relaxation of the form $1 - \exp(-t/\tau)$ (or for antipolarizing cells $\exp(-t/\tau)$). By contrast, curves related to *no*
217 *polarization* show no evolution over 40 min and are centered around $I_{pol} = 1$.

218 From the plateauing exponential curves of *polarization* and *anti-polarization* events (**Fig. 5 B-C**), one can extract the
219 characteristic times τ of the respective kinetics (**Fig. 5D** and **E**). This time is inversely related to the rate of polarization,
220 i.e. larger values of τ indicate slower kinetics. Figure 5D shows similar characteristic times for cluster⁻/Antigen^{low}
221 and cluster⁻/Antigen^{high} droplets, meaning that, independently of the antigen concentration, once the polarization is
222 triggered, it reaches a plateau within 15 min (mean value). This suggests that polarization kinetics do not depend on the
223 initial antigen concentration, as long as these conditions are sufficient to initiate polarization. By contrast, characteristic

224 times are significantly different for stiffer versus softer droplets, suggesting that stiffness affects the polarization dynamics:
 225 B cells polarize faster in the case for a stiffness of about 12 kPa than 30 kPa. Noteworthy, polarization is faster when
 226 droplets allow accumulation of antigens at the synapse (at equal conditions, see stiffness^{high}/cluster⁺/Antigen^{low} vs
 227 stiffness^{high}/cluster⁻/Antigen^{high}). Although the differences in some cases are not significant (most likely due to low
 228 statistics of anti-polarization cell subpopulations), similar tendency is found in antipolarizing behavior.
 229 Altogether, these results reveal that B cells are dynamically mechano-sensitive, as they are able to discriminate stiffness
 230 changes, and significantly adjust the polarization rate according to the apparent stiffness of the substrates they face. Also,
 231 accumulating antigens at the synapse allow cells to polarize as fast as on softer (stiffness^{medium}) substrates. Therefore,
 232 the local antigen concentration is an important feature to induce an efficient polarization, suggesting a synergistic role of
 233 low stiffness and antigen mobility in accelerating lysosome polarization.

Droplet condition	Oil phase	Surf.tension (mN/m) [pendant drop]	Stiffness (kPa)	Functionalization type	Observed Ag. enrichment	Antigen concentration	Droplet size (mean±sd) (μm)	Polarization	No polarization	Anti-polarization
(i)	Mineral oil Oleic acid 5%v/v	1.7	4.0	Surface	No	100	11.06 ± 0.88	+	+++	+
(ii)	Mineral oil	4.7	11.7	Surface	No	100	10.04 ± 1.92	+++	+	++
(iii)	Soybean oil	12	29.8	Surface	No	100	11.0 ± 0.7	+++	+	++
(iv)	Soybean oil	12	29.8	Surface	No	50	11.0 ± 0.7	+	++	+
(v)	Soybean oil	12	29.8	Bulk	Yes	50	11.30 ± 2.88	++	+	++
Control - BSA	Soybean oil	12	29.8	Bulk	No	-	11.30 ± 2.88	-	+++	-

Table 1. Recapitulation of droplet conditions, properties and outcomes.

234 Discussion

235 In this work we introduced a new material to activate B cell: lipid-coated droplets. We characterized the physical and
 236 chemical properties of functionalized droplets and studied their effect on lysosome polarization in B cells. We could prove
 237 that these objects are able to activate B cells and that the onset of polarization is sensitive to ligand concentration and
 238 droplet apparent stiffness. This is consistent with previous observations showing that lysosome polarization, necessary
 239 for protease secretion, antigen degradation and extraction (13), occurs predominantly on non-deformable/stiff substrates,
 240 where mechanical internalization is not possible (15). We could not access whether there is antigen internalization
 241 from the droplets. However, in a recent work we show that there is, at least on stiff droplets, exocysts enrichment at
 242 the synapse, a signature of proteases release (44). Future efforts will be directed to make droplets where mechanical
 243 extraction is possible.

244 We showed that B cells polarize only when they interact with substrates presenting a surface tension greater than 4.7
 245 mN/m (corresponding to an apparent stiffness of 11.7 kPa). This is consistent with observation on macrophages and fol-
 246 licular dendritic cells (15). Of note, the stiffest (11.7 and 29.8 kPa) and softest (4.0 kPa) droplets induce responses similar
 247 to, respectively, follicular dendritic cells and dendritic cells (15). We propose that this is linked to the BCR mechano-sensi-
 248 tivity. Indeed, BCR signal is known to depend on the substrate stiffness (6) and the signal downstream the BCR to induce
 249 the accumulation of polarity cues (3, 12, 16). These polarity cues establish the pole by anchoring the centrosome (45),
 250 reorienting the microtubule based traffic towards the synapse: the stronger the signal, the stronger the establishment
 251 of polarity cues, the higher the probability of polarizing. Unexpectedly, we also found that the kinetic of polarization is
 252 sensitive to the model APC stiffness. Mechano-sensitivity of dynamical properties has been shown in adhesive cells: actin

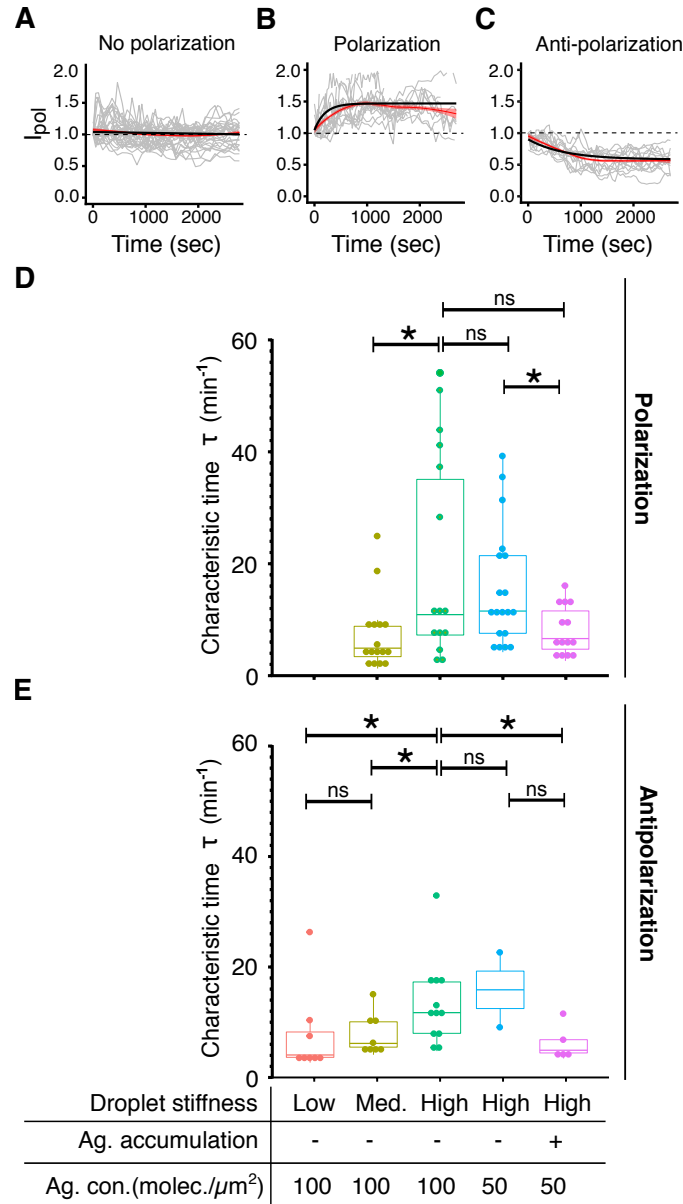


Fig. 5. B cell polarization kinetics depends on the mechanical properties of the droplets. (A-B-C) Kinetics of polarization in the three types of behavior for the (A) non-polarized $\text{Stiffness}^{\text{low}}/\text{cluster}^-/\text{Antigen}^{\text{high}}$ condition (N=28 cells), polarized $\text{Stiffness}^{\text{medium}}/\text{cluster}^-/\text{Antigen}^{\text{high}}$ condition (N=16), and anti-polarized $\text{Stiffness}^{\text{high}}/\text{cluster}^-/\text{Antigen}^{\text{high}}$ condition (N=13) cells (from at least 3 independent experiments). Fitting curves of I_{pol} (black solid curves) for polarized cells and anti-polarized cells respectively follow $y_{\text{pol}} = (p-1)(1 - \exp(-t/\tau)) + 1$ and $y_{\text{antipol}} = (1-p)(1 - \exp(-t/\tau)) + 1$ (with τ characteristic times of polarization/anti-polarization kinetics). Red shaded curves represents the average values of dynamics at each time point and their 95% confidence interval. (D) Characteristic times of polarization and (E) anti-polarization kinetics (Mann-Whitney tests). $\text{Stiffness}^{\text{low}}$, $\text{Stiffness}^{\text{medium}}$ and $\text{Stiffness}^{\text{high}}$ denotes quantitative stiffness of respectively 4.0, 11.7 and 29.8 kPa. Antigen concentration relative to 100 and 50 antigens/ μm^2 denotes respectively $\text{Antigen}^{\text{high}}$ and $\text{Antigen}^{\text{low}}$. p-values: * $p < 0.05$ and ns: not significant.

253 flows increase with the rigidity of the substrate (46), cells adjust their contractility in real time to the stiffness change of
254 the substrate (47), and T cells adapt their pulling force at the synapse to the stiffness of the interacting object (48, 49).
255 One explanation for the dependency of polarization kinetics on the mechanics of the substrate, could be that the increase
256 in stiffness downstream of the BCR activation (see e.g. (50)), hinders the displacement of the centrosome and hence
257 the polarization of lysosomes, effectively lowering the polarization rate on the stiffest substrates. Although we have no
258 direct readout of the signal, it is interesting to compare this results with recently published data on cytotoxic granules
259 release in CD8+ T cells (4): in this case the stronger the signal, the highest the frequency of polarizing cells. However,
260 the kinetics of polarization does not seem to be influenced by the strength of the signal. Future investigations on the
261 relation between signal, rheological changes and polarization following BCR activation will better highlight differences and
262 analogies between the two lymphocytes.

263 We quantified the statistics of cell polarization when they were able to accumulate antigens at the contact zone or not,
264 and to interact with 50 to 100 antigens/ μm^2 . Our results showed that the maximal amount of polarized cells is reached
265 for 75 antigens/ μm^2 , suggesting that above this density, antigen concentration has no effect on the polarization process.
266 This value is compatible with the maximal density of BCRs available in an activated synapse ¹. In addition, previous
267 work reported that antigen concentration from 15 to 150 antigens/ μm^2 modulates the B cell activation with a threshold
268 that depends on the affinity (10). Although we cannot quantitatively compare these results to ours (different antigens and
269 presentation assays), this suggests the concentration threshold for polarization might also depend on the antigen affinity.
270 Further experiments will better elucidate the link between early signaling, lysosome polarization, and antigen affinity.
271 Other works have shown that B cells interacting with mobile ligands displayed significantly greater signaling because of
272 the formation, the accumulation, and the merging of BCRs microclusters (11, 42, 52). We herein show that lysosomes
273 polarize independently of the ability to form a central antigen cluster. We showed, however, that “mobility”, allowing the
274 local increase of antigen concentration at the synapse, helps B cells overcome the low initial antigen concentration (below
275 75 antigens/ μm^2), increases the chance for a cell to polarize and its polarization rate. This suggests that local antigen
276 concentration is at the synapse is a crucial feature for inducing polarization and make it quicker.

277 One interesting aspect of our system is to allow stimulation of B cells using the same presentation assay, that combines a
278 fluid (such as bilayers) and soft material (such as gels) to investigate new synergies. In addition, the droplets are a highly
279 reproducible and well-calibrated tool in terms of chemical and mechanical properties (compared e.g. to beads or gels),
280 which makes them adapted to study cell-to-cell variability. This has allowed us to show that in clonal B cell lines, not all
281 cells polarize their lysosome towards the synapse, but some even displace them in the opposite side of the synapse (anti-
282 polarize). In T lymphocytes, a transient anti-polarization of actin and myosin has been observed in the early stage of the T
283 cell/APC contact, and does not depend on antigen recognition (53). By contrast, B cell anti-polarization is stable (over 40
284 min), BCR specific and is only triggered above 75 antigens/ μm^2 . Interestingly, the stiffness does not influence the onset
285 of anti-polarization. Like the polarization process, antigen mobility and concentration does not affect the anti-polarization

¹This number comes from an estimation that considers: 20000 receptors (IgM in primary cells) (51) squeezed in a synaptic region of radius $7\mu\text{m}$: $20000/\pi 7^2 \approx 130 \text{ mol}/\mu\text{m}^2$ interacting with bivalent ligands.

286 kinetics, but stiffness does. Of note, we observed that anti-polarized cells are more elongated and considerably less
287 round than the polarizing or non responsive ones. Similar events have been described in frustrated T cell-APC conjugates
288 (54), where the centrosome is blocked behind the nucleus while membranes accumulate at the synapse, which ultimately
289 deforms the cell. Alternatively, the anti-synapse might represent a signaling complex in its own right as already described
290 in T cells (53). Further comparison of the proteins implicated in the proximal and distal poles, both during the polarization
291 and the anti-polarization formation, would elucidate this latter suggestion.

292 Compared to existent antigen presenting surfaces, our method allows us to modify fluidity, concentration and stiffness
293 on the same material. While we achieved similar results as on bilayers (for concentration/ fluidity) and rigidity threshold
294 for activation, we will investigate more thoroughly (e.g. looking at signal magnitude) the interplay between the different
295 properties in a future work. Our method allowed us to precisely phenotype lysosome polarization dynamics. This may be
296 combined with classic (genetic or pharmacological) perturbations to dissect single cell polarization mechanisms in real
297 time and further understand the biological significance and functions of the phenotypes we described. We anticipate that
298 this approach will be of interest in many other contexts, where cell-cell variability is important for the immune function such
299 as T cell immune synapses (55), cytotoxic cell encounter (56, 57), and phagocytosis (23, 58).

300 **Materials and methods**

301 **Materials**

302 Pluronic F-68 (Ploxamer 188, CAS no. 9003-11-6), sodium alginate (CAS no. 9005-38-3), Tween 20 (polyethylene glycol
303 sorbitan monolaurate, CAS no. 9005-64-5), oleic acid (CAS no. 112-80-1, ref. O1008), silicone oil (viscosity 350 cSt at
304 25°C, CAS no. 63148-62-9) and mineral oil (light oil, CAS no. 8042-47-5) were purchased from Sigma-Aldrich (Saint
305 Quentin Fallavier, France). DSPE-PEG₂₀₀₀-Biotin lipids (1,2 - distearoyl - sn - glycerol - 3 - phosphoethanolamine - N
306 - [biotinyl (polyethyleneglycol) - 2000] ammonium salt, CAS no. 385437-57-0) were purchased from Avanti Polar Lipids
307 (Alabaster, AL, U.S.A). FluoProbes 488 streptavidin (ref. FP-BA2221) and Biotin-SP (long spacer) AffiniPure F(ab')₂
308 Fragment Goat Anti-Mouse IgG, F(ab')₂ fragment specific (min X Hu, Bov, Hrs Sr Prot) (CAS number: 115-066-072) were
309 respectively purchased from Interchim (Montluçon, France) and Jackson ImmunoResearch (Ely, U.K.). Ultrapure water
310 (Millipore, 18.2 M.Ω) was used for all experiments. All reagents and materials were used as purchased, without any
311 further purification. Lipiodol (CAS no. 8002-46-8) was kindly provided by the company Guerbet (Villepinte, France).

312 **Cell culture**

313 Mouse IgG+ B-lymphoma cell lines IIA1.6 (31), derived from A20 cell lines (ATTC# TIB-208), were cultured at 37°C in
314 a 5% CO₂ atmosphere in CLICK medium (RPMI 1640 Medium GlutaMAX™ Supplement, ref. 61870036; supplemented
315 with 10%v/v decompemented fetal calf serum, ref. 16140063; 1%v/v antibiotic Penicillin-Streptomycin, ref. 15070063;
316 2%v/v sodium pyruvate at 100 mM, ref. 11360070; and 0.1%v/v 2-Mercaptoethanol at 50 mM, ref. 31350010). All these
317 reagents were purchased from Life Technologies - Gibco. Experiments were performed with cell densities close to 10⁶
318 cells/mL, which were diluted to ca. 200 000 cells/mL and split in 10 samples of 1 mL, inserted in a 12-well plate (Falcon, ref.

319 353043). For each experiment, a 1 mL cell sample and 25 μL of HEPES (4- (2-hydroxyethyl) - 1- piperazineethanesulfonic
320 acid, Gibco) were put in a 1.8 mL tube compatible with the pressure controller (Fluigent, France). In the meantime, other
321 samples remained incubated at 37°C, 5% of CO₂ for a maximum of 4h.

322 Cell staining

323 Lysosomes were stained by loading the cells with LysoTracker™ Red DND-99 (1 mM, ref. L7528) at a final concentration
324 of 50 nM purchased from Life Technologies | Thermo Fisher Scientific (Invitrogen), into CLICK Medium, 37°C, 5% CO₂
325 for 30 min. The cell concentration is about 0.5 M cells/mL.

326 Bulk droplet functionalization protocol with phospholipids

327 The lipid-containing oil was obtained by dilution of DSPE-PEG₂₀₀₀-Biotin phospholipids (Avanti Lipids, Alabama, USA)
328 in soybean oil at 0.03 mg/mL, followed by 30 min of sonication and evaporation of the chloroform from the oil at room
329 temperature. This oil was dispersed and emulsified by hand in an aqueous continuous phase containing 15% w/w of
330 Pluronic F68 block polymer surfactant and 1% w/w sodium alginate (Ref : W201502, Sigma Aldrich, St. Louis, MO, USA)
331 at a final oil fraction equal to 75% w/w. The rough emulsion was then sheared in a Couette cell apparatus at a controlled
332 shear rate following the method developed by Mason *et al.* (59) to narrow the droplet size distribution to $12.4 \mu\text{m} \pm 2.3$
333 μm (**Table 1**). For storage, emulsions are diluted to an oil fraction of 60 wt % with 1 wt % Pluronic F68 in the continuous
334 phase and stored at 12°C in a Peltier storage cupboard for several weeks.

335 Surface Droplet Functionalization Protocol with Phospholipids

336 Droplets were formulated using a Shirasu Porous Glass apparatus (SPG Technology Co., Japan) by extruding the oil
337 phase (with or without 5%v/v of oleic acid) through a ceramic membrane (with pores of 3.1 μm , SPG Technology Co., Ltd)
338 within an aqueous solution containing 15%v/v of Pluronic F68, continuously and vigorously stirred. We obtained droplets
339 measuring $10.98 \pm 0.68 \mu\text{m}$ in diameter. Once stabilized, droplets were washed out 3 times with an aqueous solution of
340 Tween 20 at CMC (0.0007% w/v). The supernatant was removed and replenished after each centrifugation step (30 sec
341 at 2000 RPM). The suspension is centrifuged and rinsed four times with phosphate buffer (PB)/ Tween 20 to decrease the
342 amount of Pluronic F68 in the continuous phase. After the last rinsing step, most of the continuous phase is removed from
343 the microtube to decrease the total volume of emulsion to 10 μL . We then add 10%v/v of the DMSO stock solvent solution
344 containing the phospholipids. We then add a phosphate buffer supplemented with Tween 20 at the CMC (PB - Tween 20)
345 to reach a total volume of 200 μL of suspension. Droplets are incubated for 30 min at room temperature in the presence
346 of lipids in the bulk phase and finally rinsed several times with a PB - Tween 20 buffer to remove the phospholipids in
347 excess. The quantity of phospholipids available in the bulk phase at the initial stage is adjusted by diluting the stock
348 solutions in DMSO so that the volume fraction of co-solvent remains constant for all experimental conditions. For a given
349 working volume (200 μL), the lipid concentration in the bulk phase is expressed as a droplet surface area equivalent.
350 One equivalent (eq.) corresponds to the number of molecules required to cover the total area of a droplet sample with a
351 compact monolayer (33).

352 **Coating of Biotinylated Droplets with Streptavidin and F(ab')₂ fragments**

353 After the first step of emulsification and insertion of biotinylated lipids at the interface, 1 equivalent of streptavidin solution
354 at 1 mg/mL was added, followed by an incubation time of 30 min and a washing step to remove all excess streptavidin.
355 Finally, 1 equivalent of F(ab')₂ fragments (1 mg/mL) or BSA (1 mg/mL) was added to the droplet solution, followed by
356 an incubation time of 30 min and a washing step to remove all excess F(ab')₂ or BSA. One equivalent (1 eq.) of a
357 given macromolecule (lipid or protein) corresponds to the theoretical number of molecules needed to cover the entire
358 surface with a monolayer of molecules or proteins, considering the available surface of droplet and molecule dimensions
359 as previously reported in (33).

360 **Measurement of the adsorption isotherms of the surface-functionalized droplets**

361 To quantify the amount of antigens presented by droplets, we first titrated the antigens (from 0.05 to 5 eq.) bound
362 to streptavidin molecules (1 eq.) and biotinylated DSPE-PEG₂₀₀₀ lipids (100 eq.). We revealed the antigens coating
363 with a Donkey anti-Goat IgG (H+L) Cross-Adsorbed Secondary Antibody (Alexa Fluor 647, Invitrogen, ref. A-21447) and
364 analyzed the fluorescence intensity. In our case, the droplets are saturated for 4 eq. of F(ab')₂ fragments (**Supplementary**
365 **Note 2**). We then converted this relative concentration into absolute value by comparing fluorescence intensity of droplets
366 and commercial tagged beads (Quantum™ MESF, Bang Laboratories, Inc.). We assessed the related fluorescence
367 intensities of droplets coated with a concentration of streptavidin ranging from 0 to 2 eq. and saturated in biotinylated
368 DSPE-PEG₂₀₀₀ lipids (100 eq.) (**Supplementary Note 2**). These values are added on a calibration curve correlating
369 the molecular equivalent surface fluorescence (MESF) of beads (Quantum™ MESF, Bang Laboratories, Inc.) with their
370 fluorescence intensities (**Supplementary Note 2** and **Fig. S4**). Finally, we converted the droplet MESF into absolute
371 values of F(ab')₂ fragments in antigens per μm^2 (**Fig. 2D**) depending on different droplet and protein features. We
372 obtained that droplets present from 0 to 150 antigens/ μm^2 when they are functionalized with DSPE-PEG₂₀₀₀-Biotin (100
373 eq.), streptavidin from 0 to 2 eq. and F(ab')₂ fragments (4 eq.). For the rest of the experiment, we use droplets coated
374 with 50 and 100 antigens/ μm^2 . Fluorescence measurements in **Fig. S6** have been performed using Alexa Fluor® 647
375 Mouse IgG1, κ Isotype Ctrl (ICFC) Antibody, Biologend 400135, at a concentration of 0.5 eq.

376 **Measurement of oil/water interfacial tension by the pending drop technique**

377 The pendant drop technique consists in inferring the interfacial tension from the shape profile of a pendant drop of one
378 liquid in another at mechanical equilibrium. We used a pending drop apparatus (drop shape analyzer, Krüss, PSA30)
379 to measure the interfacial tension of the various oils considered in this study - mineral oil, mineral oil supplemented with
380 5%v/v of oleic acid, soybean oil, lipiodol and lipiodol supplemented with 5%v/v of oleic acid - versus an aqueous solution
381 composed of 15%w/w Pluronic 68. The interfacial tensions reported in **Table S1** correspond to the equilibrium value
382 reached when the drop surface has been entirely covered by surfactants coming from the continuous phase.

383 **Measurement of droplets interfacial tension by the micropipette technique**

384 The micropipette-aspiration method that has been described in detail in a previous article (38). Micropipettes were made
385 from 1 mm borosilicate glass-tube capillaries (Harvard Apparatus, USA) that were pulled in a pipette heater and puller
386 (P-2000, Sutter instrument Co., USA) to tip diameters in the range of 3 to 5 μm . A 3 axis-micromanipulator (Narishige)
387 allowed for pipette positioning and manipulation. The pipette was connected to a pressure controller (Fluigent) to apply
388 precise negative pressures. A solution of sinking droplets, made with lipiodol oil coated or not with phospholipids, was
389 inserted into a glass/coverslip chamber. The pipette aspirated the droplet until reaching an equilibrium where the elongation
390 part is equal to the pipette inner dimension. The interfacial tension γ is $\gamma = \Delta P \cdot (R_p/2)$ where ΔP is the negative pressure
391 and R_p the micropipette radius. Upon aspiration by the very thin glass pipette, the droplet deforms and a spherical cap of
392 radius R_c forms at the tip of the pipette. At equilibrium, the value of R_c depends on the interfacial tension γ of the droplets,
393 the radius of the droplet R_D , the aspiration pressure ΔP and can be expressed as:

$$\frac{1}{R_c} = \frac{\Delta P}{2\gamma} + \frac{1}{R_D} \quad (1)$$

394 The aspiration ΔP corresponds to the pressure difference between the inside of the pipette and the external pressure. γ
395 and R_p are constant throughout the experiment. Hence, varying ΔP induces changes in R_c : the larger ΔP , the smaller
396 R_c . During measurements, ΔP is slowly increased and R_c decreases until reaching the radius of the pipette R_p . Up to
397 that critical aspiration ΔP_c , little change is observed in the geometry of the system. As soon as ΔP becomes greater
398 than ΔP_c , R_c becomes smaller than R_p , which results in the sudden entry of the oil droplet in the pipette. This provides a
399 direct measurement of the surface tension of the droplet:

$$\gamma = \frac{\Delta P_c}{2 \left(\frac{1}{R_D} - \frac{1}{R_p} \right)} \quad (2)$$

400 The interfacial tensions reported in **Table S2** have been measured via micropipette on phospholipid-functionalized
401 and non-functionalized droplets. Droplets are stabilized by F68 and bathed into an aqueous phase made of phosphate
402 buffer/Tween 20 at CMC.

403 **Measurement of droplet mechanical properties by the microplate rheology**

404 The microplate micro-rheology experiment consists in applying a sinusoidal displacement to the base of a flexible mi-
405 croplate $B(t) = B_0 e^{i\omega t}$ (with elastic constant k) and measuring the resulting amplitude T_0 and the phase shift ϕ of the
406 flexible microplate tip in contact with the droplet (see **Fig. 2F**). Of note, the offset of the microplate applies a strain of 2 μm
407 and the oscillation amplitude of 1 μm is applied around this point. The droplet complex dynamic modulus G^* is obtained
408 from the applied oscillatory normal stress. Microplates were made from glass lamellae of 100 x 2mm with 0.1-0.3 mm
409 thickness. The rigid plate can be either pulled out of 0.2 or 0.3 mm original thickness, but must be kept short to ensure a
410 high stiffness. Lamellae were heated and pulled (Narishige PB-7, Japan) until breaking in two similar parts. Microplates

411 were calibrated using a microplate of known bending stiffness as a reference. The bending stiffness of the reference
412 microplate has been initially determined by stacking copper micro-wires at the extremity of the plate, following the protocol
413 reported in (60). A microplate of low bending stiffness (flexible) acts as a spring, and a rigid plate about 1000 times stiffer
414 than the flexible one acts as support. During experiments, the flexible plate is oscillated, applying oscillating stress on the
415 studied sample and compressing it sinusoidally against the rigid plate. The flexible plate was oscillated from 0.1 to 6.4Hz
416 for droplets and until 1.6 Hz for cells. Micrometric displacements of plates are controlled via highly-resolutive piezoelectric
417 micromanipulators. The deflection δ of the flexible plate is related to the force F exerted on the sample by $F = k\delta$ where
418 k is the bending stiffness of the flexible plate. The deformation of the sample is $\epsilon = (L_0 - L)/L_0$ where L_0 is the resting
419 cell or droplet diameter. For mechanical characterization, we used the dynamic analysis protocol consisting in applying a
420 controlled sinusoidal stress or strain at different frequencies on the cell, while measuring the complementary visco-elastic
421 response provided by the droplet or cell (60). For droplet experiments, Lipiodol (Guerbet) oil (that sediment being denser
422 than water) was used to fabricate droplets and glass microplates were coated with PLL at 0.1%v/v. For cells, only the
423 chamber was coated with Sigmacote (Sigma-Aldrich).

424 **Measurement of diffusion coefficient - FRAP experiments**

425 Droplets have been coated with DSPE-PEG-Biotin/streptavidin and F(ab)₂' and then image with a spinning-disk confocal
426 microscope Nikon Eclipse 2 equipped with a Yokogawa CSU head, objective Apochromat 63X NA1.3. Droplets were
427 photobleached with circular ROIs of $D = 2.5, 5.1$ and $8.8 \mu\text{m}$ at the top of their surface following (61). Movies of the
428 recovery were taken with a frame rate of 30 s before and after a photobleaching pulse of 150 ms. Experiments were
429 performed at 37°C. The recovery time was inferred from exponential fit of the measured intensity. The diffusion coefficient
430 was extracted from a linear fit of the mean of the measured times at different radius (61).

431 **Design and microfabrication of the microfluidic trapping array**

432 Microfluidic chips were designed on CleWin (WieWeb Software). The double layer technique required the creation of two
433 masks: traps and pillars. Chrome masks were fabricated with the μPG 101 maskless aligner (Heidelberg Instruments
434 Mikrotechnik GmbH), and the final silicon mold with the MJB4 aligner system (Karl Süss). Two SU8 photoresists (Mi-
435 crochem) have been used, 2005 and 2010 to respectively obtain $5 \mu\text{m}$ -thick pillars and $10 \mu\text{m}$ -thick traps. To avoid any
436 PDMS sticking to the small SU8 structures and long-term mold damage, we coated the wafer with a fluorinated silane by
437 vapor deposition (trichloro (1H,1H,2H,2H-perfluorooctyl) silane, CAS: 102488-49-3, Merck-Sigma-Aldrich). Liquid PDMS
438 (RTV 615, Momentive Performance) at a base:crosslinker 1:10 ratio was poured on the silicon-SU8 mold and cured for
439 more than 2h at 70°C to complete the crosslinking. After cutting PDMS pieces and punching out inlets and outlets with
440 a biopsy puncher (OD = 0.75 mm, Electron Microscopy Sciences, Hatfield, UK), the top PDMS part was bonded to a
441 glass-bottom Petri dish (FluoroDish FD35-100, WPI) together after a O₂ plasma treatment of both surfaces (50 W for 30 s,
442 20 sccm O₂ flow, 0.15 torr pressure, Cute Plasma oven, Femto Science, Korea), and left for 30 sec at 90°C to improve the
443 bonding. For a long-term hydrophilic coating (Hemmila, 2012) of the inner PDMS channels, a 0.25 wt% polyvinylpyrrolid-

444 done (PVP, K90, Sigma Aldrich) solution was injected in the chip. Finally, the chip channels were rinsed with culture media
445 before inserting droplets and cells.

446 **Experimental setup for the cell-droplet encounters**

447 By connecting the microfluidic devices to a pressure controller, a fixed pressure drop ΔP between the inlet and the outlet
448 of the chamber is set (maximum 1000 Pa, corresponding to a fluid velocity of 1.6 mm/s). Traps are initially rinsed with
449 CLICK medium during at least 5 min. Then, 200 μL of the droplets suspension (10^6 droplets/mL in CLICK medium) are
450 inserted in the microchip using the pressure regulator. Once a desired number of droplets is trapped, the first tubing is
451 carefully removed and replaced by the tubing connected to the B cell-containing tube. Different positions and focus are
452 marked and cells are progressively inserted at a maximum speed of 1.6 mm/s while the acquisition is launched. To avoid
453 a saturation of traps in cells while ensuring culture medium replenishment, the flow is lessened at 0.4 mm/s. Particle
454 displacements and trapping are observed by video-microscopy.

455 **Microscopy-Imaging of B cell polarization dynamics**

456 Brightfield and fluorescent images of the synapses are acquired on a Leica DMI8 microscope (Germany) connected to
457 an Orca Flash4.0 sCMOS camera (Hamamatsu Photonics, Japan). Epi-illumination is done with a LED light (PE-4000,
458 CoolLED) and a GFP filter set (Excitation/Emission: 470/525 nm) for the fluorescent coated droplets, and a TexasRed
459 filter set (Excitation/Emission : 561/594 nm) for the fluorescent cells. Time zero of the experiment is defined manually
460 when a cell encounters a droplet. All pictures of cell-droplet pairs were imaged with a 40x objective (Leica, dry, N.A.=0.8,
461 Framerate : 50 sec.).

462 **Image Analysis**

463 Image analyses were performed with ImageJ/ Fiji (62) (version 1.52i), and data analyses were performed with R (RStudio)
464 software (version 2). For all processes, 16-bit images were analyzed. Codes are available on request.

465 **Quantification of antigen recruitment**

466 The recruitment index is defined as the ratio between the fluorescence intensity over time $I(t)$ divided by the fluorescence
467 intensity at the initial time $I(0)$, both at the synapse area. The synapse area is counterered by hand for each time point. The
468 maximum and mean fluorescence intensities were measured at each time point (from time zero to 40 min).

469 **Quantification of lysosome polarization and cell classification**

470 Each cell shape was contoured by hand for each time point (from time zero to 40 min) and using a ImageJ macro,
471 automatically divided in two parts according to the main orientation of the cell-droplet pair. It extracted the fluorescence
472 intensity at the middle front side of the cell (in contact with droplet) $I_{front}(t)$ and at the back of the cell $I_{back}(t)$ at each
473 time point, and computed the polarization index defined as $[I_{front}(t)/I_{back}(t)] \times [I_{back}(0)/I_{front}(0)]$ (**Fig. 4D**). To classify
474 the cells we noticed that most of I_{pol} curves reach a plateau, hence focused on the final I_{pol} defined as averaged over last

475 5 minutes (in the rare case where this was not possible as the polarization kinetics followed a non-plateauing growth we
476 considered only the last time point.). Transient polarizing cells were not classed as polarized.

477 Numerical simulations

478 The numerical simulations are performed with COMSOL Multiphysics ®(version 5.3). We first developed a two-
479 dimensional depth-averaged computational fluid dynamics - finite element model of the microfluidic chamber with exactly
480 the same approach that the one proposed in (63). We consider a planar and incompressible flow, at steady state, and
481 a Newtonian fluid with a dynamic viscosity of $\mu = 10^{-3}$ Pa.s. Hence, the equation set verified inside the fluid domain is
482 written as $-\nabla P + \mu \Delta v + f_v = 0$ and $\nabla \cdot v = 0$, where P is the pressure field, v the velocity field and f_v the volume force.
483 In addition, the non-slip condition on the out-of-plane walls is considered with a Darcy's law (also called "shallow channel
484 approximation") thus follows $f_v = -12\mu/d^2 v$.

485 On physical walls, a non-slip boundary condition is added. The pressure is set as uniform both at the inlet and outlet. This
486 pressure is equal to the pressure drop in the chamber or equal to 0 Pa, respectively at the inlet and outlet. Finally, we
487 deduced the pressure drop through a single trap ΔP_{trap} from the isobar lines plot (**Supplementary Note 1**).

488 A 3D model focused on the geometry of one trap. We used the same hypotheses and set of equations than the previously
489 detailed 2D model except that we do not consider Darcy's law, thus we consider a non-slip condition on the upper and
490 lower faces of the chamber as $f_v = 0$. On the inlet, the pressure is set as uniform and equal to ΔP_{trap} while on the outlet,
491 it is considered as uniform and equal to 0 Pa. Finally, we considered the flow as symmetric on the boundary linking with
492 the rest of the microfluidic chamber.

493 Statistical analysis

494 All statistical analysis have been performed using Prism GraphPad (version 8) and R programming language. Codes are
495 available on request. Tests and p -values are specified in the figures.

496 Data availability

497 ImageJ macro, R code and microfluidic trap designs are available in the following GitHub folder:
498 <https://github.com/FattaccioliLab/PhenotypingBCellsWithLipidDroplets>.

499 Supplementary Information

- 500 • Supplementary Notes : 1 - 4
- 501 • Supplementary Figures : Fig S1 – S10
- 502 • Supplementary Tables : Table S1 – S3
- 503 • Supplementary Movies : Movie S1 – S3

504 ACKNOWLEDGEMENTS

505 The authors thank A.M Lennon-Duménil for scientific support and critical reading of the manuscript, thank the company Guerbet for having kindly provided Lipiodol®oil
506 samples, F. Pincet, D. Langevin, B. Cabane and J. Voldman for helpful discussions, P. Saez for cell culture advice and O. Ait-Mohamed for help with statistical analysis. This

507 work benefited from the technical contribution of the Institut Pierre-Gilles de Gennes joint service unit CNRS UAR 3750. The authors would like to thank the engineers of this
508 unit for their advice during the development of the experiments. The authors are grateful to H. Moreau, J. Brujic, M. Thery and R. Dreyfus for critical reading of the paper and
509 suggestions.

510 AUTHOR CONTRIBUTIONS

511 L.P., P.P. and J.F. designed the study. L.P. performed all the experiments and analyzed experimental results. N.R. and R.A. conducted all simulation studies. O.M. carried out
512 preliminary experiments on microfluidics and cell culturing. J.P. helped during microfluidics and cell culturing experiments. D.C. made the micropipette setup and contributed
513 to the experiments. A.C. and C.L.G. helped with Imagestream experiments described in the answer to the referees. S.A. and A.A. performed all microplate experiments,
514 analyzed experimental results and wrote the manuscript. L.P., P.P. and J.F. wrote the manuscript. All authors approved the final version of the article.

515 FUNDINGS

516 L.P., N.R. and J.P. were respectively funded by the IPV scholarship program (Sorbonne Université), the *École Normale Supérieure de Rennes*, and the Bettencourt scholarship
517 program (CRI-FIRE). J.F. acknowledges funding from the Agence Nationale de la Recherche (ANR Jeune Chercheur PHAGODROP, ANR-15-CE18-0014-01).

518 COMPETING FINANCIAL INTERESTS

519 No competing financial interests

520 Bibliography

- 521 1. Johannes B. Huppa and Mark M. Davis. T-cell-antigen recognition and the immunological synapse. *Nature Reviews Immunology*, 3(12):973–983, 2003. ISSN 14741733. doi: 10.1038/nri1245.
- 522 2. M.-I. Maria-isabel Yuseff, Paolo Pierobon, Anne Reversat, and A.-M. Lennon-Duménil. How B cells capture , process and present antigens : a critical role for cell polarity Antigen encounter and the
523 role of presenting Cells. *Nature Reviews Immunology*, 13(July):475–486, 2013. ISSN 14741733. doi: 10.1038/nri3469.
- 524 3. Karen L. Angus and Gillian M. Griffiths. Cell polarisation and the immunological synapse. *Current Opinion in Cell Biology*, 25(1):85–91, 2013. doi: 10.1016/J.CEB.2012.08.013.
- 525 4. Gordon L. Frazer, Christian M. Gawden-Bone, Nele M.G. Dieckmann, Yukako Asano, and Gillian M. Griffiths. Signal strength controls the rate of polarization within CTLs during killing. *Journal of*
526 *Cell Biology*, 220(10), 2021. ISSN 15408140. doi: 10.1083/jcb.202104093.
- 527 5. F. D. Batista and M. S. Neuberger. Affinity Dependence of the B Cell Response to Antigen: A Threshold, a Ceiling, and the Importance of Off-Rate. *Cell Press*, 8:751–759, 1998.
- 528 6. Z. Wan, S. Zhang, Y. Fan, K. Liu, F. Du, A. M. Davey, H. Zhang, W. Han, C. Xiong, and W. Liu. B Cell Activation Is Regulated by the Stiffness Properties of the Substrate Presenting the Antigens.
529 *The Journal of Immunology*, 190(9):4661–4675, 2013. ISSN 0022-1767. doi: 10.4049/jimmunol.1202976.
- 530 7. Samina Shaheen, Zhengpeng Wan, Zongyu Li, Alicia Chau, Xinxin Li, Shaosen Zhang, Yang Liu, Junyang Yi, Yingyue Zeng, Jing Wang, Xiangjun Chen, Liling Xu, Wei Chen, Fei Wang, Yun Lu,
531 Wenjie Zheng, Yan Shi, Xiaolin Sun, Zhanguo Li, Chunyang Xiong, and Wanli Liu. Substrate stiffness governs the initiation of B cell activation by the concerted signaling of PKC β and focal adhesion
532 kinase. *eLife*, 6:1–29, 2017. ISSN 2050084X. doi: 10.7554/eLife.23060.
- 533 8. Christina M. Ketchum, Xiaoyu Sun, Alexandra Suberi, John T. Fourkas, Wenxia Song, and Arpita Upadhyaya. Subcellular topography modulates actin dynamics and signaling in B-cells. *Molecular*
534 *Biology of the Cell*, 29(14):1732–1742, 2018. ISSN 19394586. doi: 10.1091/mbc.E17-06-0422.
- 535 9. Y. R. Carrasco, S. J. Fleire, T. Cameron, M.I. L. Dustin, and F. D. Batista. LFA-1/ICAM-1 interaction lowers the threshold of B cell activation by facilitating B cell adhesion and synapse formation.
536 *Immunity*, 20(5):589–599, 2004. ISSN 10747613. doi: 10.1016/S1074-7613(04)00105-0.
- 537 10. S. J. Fleire, J. P. Goldman, Y. R. Carrasco, M. Weber, D. Bray, and F. D. Batista. B cell ligand discrimination through a spreading and contraction response. *Science*. 312(5774):738–741, 2006.
538 ISSN 00368075. doi: 10.1126/science.1123940.
- 539 11. Christina Ketchum, Heather Miller, Wenxia Song, and Arpita Upadhyaya. Ligand mobility regulates B cell receptor clustering and signaling activation. *Biophysical Journal*, 106(1):26–36, jan 2014.
540 ISSN 1542-0086. doi: 10.1016/j.bpj.2013.10.043.
- 541 12. Anne Reversat, Maria-Isabel Yuseff, Danielle Lankar, Odile Malbec, Dorian Obino, Mathieu Maurin, Naga Venkata Gayathri Penmatcha, Alejandro Amoroso, Lucie Sengmanivong, Gregg G
542 Gundersen, Ira Mellman, François Darchen, Claire Desnos, Paolo Pierobon, and Ana-Maria Lennon-Duménil. Polarity protein Par3 controls B-cell receptor dynamics and antigen extraction at the
543 immune synapse. *Molecular biology of the cell*, 26(7):1273–85, apr 2015. ISSN 1939-4586. doi: 10.1091/mbc.E14-09-1373.
- 544 13. M. I. Yuseff, A. Reversat, D. Lankar, J. Diaz, I. Fanget, P. Pierobon, V. Randrian, N. Larochette, F. Vascotto, C. Desdouets, B. Jauffred, Y. Bellaïche, S. Gasman, F. Darchen, C. Desnos, and A.-M.
545 Lennon-Duménil. Polarized Secretion of Lysosomes at the B Cell Synapse Couples Antigen Extraction to Processing and Presentation. *Immunity*, 35(3):361–374, 2011. ISSN 10747613. doi:
546 10.1016/j.immuni.2011.07.008.
- 547 14. E. Natkanski, Justin E. Molloy, and P. Tolar. B Cells Use Mechanical Energy to Discriminate Antigen Affinities. *Science*, 340(June):1587–1590, 2013.
- 548 15. K. M. Spillane and P. Tolar. B cell antigen extraction is regulated by physical properties of antigen presenting cells. *Journal of Cell Biology*, 2(1):1–19, 2016. ISSN 00063495. doi: 10.1016/j.bpj.
549 2016.11.701.
- 550 16. J. Wang, F. Lin, Z. Wan, X. Sun, Y. Lu, J. Huang, F. Wang, Y. Zeng, Y. H. Chen, Y. Shi, W. Zheng, Z. Li, C. Xiong, and W. Liu. Profiling the origin, dynamics, and function of traction force in B cell
551 activation. *Science Signaling*, 11(542), 2018. ISSN 19379145. doi: 10.1126/scisignal.aai9192.
- 552 17. A. Kumari, J. Pineau, P.J. Sáez, M. Maurin, D. Lankar, M. San Roman, K. Hennig, V. F. Boura, R. Votouriez, M. C. I. Karlsson, M. Bolland, A.-M. Lennon-Duménil, and P. Pierobon. Actomyosin-driven
553 force patterning controls endocytosis at the immune synapse. *Nature Communications*, 10(1):1–14, 2019. ISSN 20411723. doi: 10.1038/s41467-019-10751-7.

- 554 18. O. Thauinat, A. G. Granja, P. Barral, A. Filby, B. Montaner, L. Collinson, N. Martinez-Martin, N. E. Harwood, A. Bruckbauer, and F. D. Batista. Asymmetric segregation of polarized antigen on B cell
555 division shapes presentation capacity. *Science*, 335(6067):457–479, 2012. ISSN 10959203. doi: 10.1126/science.1214100.
- 556 19. K. Pham, F. Sacirbegovic, and S. M. Russell. Polarized cells, polarized views: Asymmetric cell division in hematopoietic cells. *Frontiers in Immunology*, 5(FEB), 2014. ISSN 16643224. doi:
557 10.3389/fimmu.2014.00026.
- 558 20. Zhengpeng Wan, Xiangjun Chen, Haodong Chen, Qinghua Ji, Yingjia Chen, Jing Wang, Yiyun Cao, Fei Wang, Jizhong Lou, Zhuo Tang, and Wanli Liu. The activation of IgM- or isotype-switched
559 IgG- and IgE-BCR exhibits distinct mechanical force sensitivity and threshold. *eLife*, 4(August):1–24, 2015. ISSN 2050-084X. doi: 10.7554/eLife.06925.
- 560 21. Hakim Boukellal, Otger Campàs, Jean-François Joanny, Jacques Prost, and Cécile Sykes. Soft $\langle i \rangle$ - $\langle f \rangle$: Actin-based propulsion of liquid drops. *Physical Review E*, 69(6):061906, jun 2004.
561 doi: 10.1103/PhysRevE.69.061906.
- 562 22. O. Campàs, T. Mammoto, S. Hasso, R. A. Sperling, O. Connell, A. G. Bischof, R. Maas, and D. A. Weitz. Embryonic Tissues. *Nature Methods*, 11(2):183–189, 2014. doi: 10.1038/nmeth.2761.
563 Quantifying.
- 564 23. K. Ben M'Barek, D. Molino, S. Quignard, M.-A. Plamont, Y. Chen, P. Chavrier, and J. Fattaccioli. Phagocytosis of immunoglobulin-coated emulsion droplets. *Biomaterials*, 51:270–277, 2015. ISSN
565 18785905. doi: 10.1016/j.biomaterials.2015.02.030.
- 566 24. L. Montel, L. Pinon, and J. Fattaccioli. A Multiparametric and High-Throughput Assay to Quantify the Influence of Target Size on Phagocytosis. *Biophysical Journal*, pages 1–12, 2019. ISSN
567 15420086. doi: 10.1016/j.bpj.2019.06.021.
- 568 25. B. Dumat, L. Montel, L. Pinon, P. Matton, L. Cattiaux, J. Fattaccioli, and J.-M. Mallet. Mannose-Coated Fluorescent Lipid Microparticles for Specific Cellular Targeting and Internalization via
569 Glycoreceptor-Induced Phagocytosis. *ACS Applied Bio Materials*, 2019. ISSN 25766422. doi: 10.1021/acsabm.9b00793.
- 570 26. N. Bourouina, J. Husson, C. HIVroz, and N. Henry. Biomimetic droplets for artificial engagement of living cell surface receptors: The specific case of the T-cell. *Langmuir*, 28(14):6106–6113, 2012.
571 ISSN 07437463. doi: 10.1021/la300398a.
- 572 27. A. M. Skelley, O. Kirak, H. Suh, R. Jaenisch, and J. Voldman. Microfluidic control of cell pairing and fusion. *Nature Methods*, 6(2):147–152, 2009. ISSN 15487091. doi: 10.1038/nmeth.1290.
- 573 28. Joon Hee Jang, Yu Huang, Peilin Zheng, Myeong Chan Jo, Grant Bertolet, Michael Xi Zhu, Lidong Qin, and Dongfang Liu. Imaging of Cell–Cell Communication in a Vertical Orientation Reveals
574 High-Resolution Structure of Immunological Synapse and Novel PD-1 Dynamics. *The Journal of Immunology*, 195(3):1320–1330, aug 2015. ISSN 0022-1767. doi: 10.4049/JIMMUNOL.1403143/
575 -/DCSUPPLEMENTAL.
- 576 29. M. Jafarnejad, M. C. Woodruff, D. C. Zawieja, M. C. Carroll, and J. E. Moore. Modeling lymph flow and fluid exchange with blood vessels in lymph nodes. *Lymphatic Research and Biology*, 13(4):
577 234–247, 2015. ISSN 15578585. doi: 10.1089/lrb.2015.0028.
- 578 30. M. Vuica, S. Desiderio, and J. P. Schneck. Differential effects of B cell receptor and B cell receptor-Fc γ RIIB1 engagement on docking of Csk to GTPase-activating protein (GAP)-associated p62.
579 *Journal of Experimental Medicine*, 186(2):259–267, 1997. ISSN 00221007. doi: 10.1084/jem.186.2.259.
- 580 31. D. Lankar, H. Vincent-Schneider, V. Briken, T. Yokozeki, G. Raposo, and C. Bonnerot. Dynamics of major histocompatibility complex class II compartments during B cell receptor-mediated cell
581 activation. *Journal of Experimental Medicine*, 195(4):461–472, 2002. ISSN 00221007. doi: 10.1084/jem.20011543.
- 582 32. Y. Zhang, A. McMullen, L.-L. Pontani, X. He, R. Sha, N. C. Seeman, J. Bruijck, and P. M. Chaikin. Sequential self-assembly of DNA functionalized droplets. *Nature Communications*, 8(1):1–7, 2017.
583 ISSN 20411723. doi: 10.1038/s41467-017-00070-0.
- 584 33. L. Pinon, L. Montel, O. Mesdjian, M. Bernard, A. Michel, C. Ménager, and J. Fattaccioli. Kinetically Enhanced Fabrication of Homogeneous Biomimetic and Functional Emulsion Droplets. *Langmuir*,
585 34(50):15319–15326, dec 2018. ISSN 0743-7463. doi: 10.1021/acs.langmuir.8b02721.
- 586 34. N. Bui, M. Saitakis, S. Dogniaux, A. Buschinger, O. and Bohneust, Al. Richert, M. Maurin, C. HIVroz, and A. Asnacios. Human primary immune cells exhibit distinct mechanical properties that are
587 modified by inflammation. *Biophysical Journal*, 108(9):2181–2190, 2015. ISSN 15420086. doi: 10.1016/j.bpj.2015.03.047.
- 588 35. Michael Saitakis, Stéphanie Dogniaux, Christel Goudot, Nathalie Bui, Sophie Asnacios, Mathieu Maurin, Clotilde Randriamampita, Atef Asnacios, and Claire HIVroz. Different TCR-induced T
589 lymphocyte responses are potentiated by stiffness with variable sensitivity. Different TCR-induced T lymphocyte responses are potentiated by stiffness with variable sensitivity. *eLife*, 6:1–29, 2017.
590 ISSN 2050084X. doi: 10.7554/eLife.23190.
- 591 36. Pierre-Gilles de Gennes, Françoise Brochard-Wyart, and David Quéré. *Capillarity and wetting phenomena*. Springer, 2004. ISBN 9781441918338. doi: 10.1007/978-0-387-21656-0_9.
- 592 37. Phil Attard and Stan J. Miklavcic. Effective Spring Constant of Bubbles and Droplets. *Langmuir*, 17(26):8217–8223, dec 2001. ISSN 0743-7463. doi: 10.1021/la010969g.
- 593 38. A. Yeung, T. Dabros, J. Masliyah, and J. Czarnecki. Micropipette: A new technique in emulsion research. *Colloids and Surfaces A: Physicochemical and Engineering Aspects*, 174(1-2):169–181,
594 2000. ISSN 09277757. doi: 10.1016/S0927-7757(00)00509-4.
- 595 39. Daniel T.N. Chen, Qi Wen, Paul A. Janmey, John C. Crocker, and Arjun G. Yodh. Rheology of soft materials. *Annual Review of Condensed Matter Physics*, 1:301–322, 2010. ISSN 19475454. doi:
596 10.1146/annurev-conmatphys-070909-104120.
- 597 40. Pei Hsun Wu, Dikla Raz Ben Aroush, Atef Asnacios, Wei Chiang Chen, Maxim E. Dokukin, Bryant L. Doss, Pauline Durand-Smet, Andrew Ekpenyong, Jochen Guck, Natalia V. Guz, Paul A.
598 Janmey, Jerry S.H. Lee, Nicole M. Moore, Albrecht Ott, Yeh Chuin Poh, Robert Ros, Mathias Sander, Igor Sokolov, Jack R. Staunton, Ning Wang, Graeme Whyte, and Denis Wirtz. A comparison
599 of methods to assess cell mechanical properties. *Nature Methods*, 15(7):491–498, 2018. ISSN 15487105. doi: 10.1038/s41592-018-0015-1.
- 600 41. N. Desprat, A. Richert, J. Simeon, and A. Asnacios. Creep function of a single living cell. *Biophysical Journal*, 88(3):2224–2233, 2005. ISSN 00063495. doi: 10.1529/biophysj.104.050278.
- 601 42. N. E. Harwood and F. D. Batista. Early Events in B Cell Activation. *Annual Review of Immunology*, 28(1):185–210, 2010. ISSN 0732-0582. doi: 10.1146/annurev-immunol-030409-101216.
- 602 43. Fulvia Vascotto, Danielle Lankar, Pablo Vargas, Jheimmy Diaz, Delphine Le Roux, Delphine le Roux, Maria-isabel Yuseff, Maria-isabel Yuseff, Jean-Baptiste Sibarita, Marianne Boes, Graça
603 Raposo, Evelyne Mougneau, Nicolas Glaichenhaus, Christian Bonnerot, Bénédicte Manoury, Ana-Maria Lennon-Duménil, Gabrielle Faure-André, Pablo Vargas, Jheimmy Diaz, Delphine le Roux,
604 Maria-isabel Yuseff, Jean-Baptiste Sibarita, Marianne Boes, Graça Raposo, Evelyne Mougneau, Nicolas Glaichenhaus, Christian Bonnerot, Bénédicte Manoury, and Ana-Maria Lennon-Duménil.
605 The actin-based motor protein myosin II regulates MHC class II trafficking and BCR-driven antigen presentation. *Journal of Cell Biology*, 176(7):1007–1019, mar 2007. ISSN 0021-9525. doi:

- 606 10.1083/jcb.200611147.
- 607 44. Judith Pineau, Léa Pinon, Olivier Mesdjian, Jacques Fattaccioli, Ana-Maria Lennon Duménil, and Paolo Pierobon. Microtubules restrict f-actin polymerization to the immune synapse via gef-h1 to
608 maintain polarity in lymphocytes. *bioRxiv*, 2022. doi: 10.1101/2022.01.03.473915.
- 609 45. Jia C. Wang, Jeff Y.J. Lee, Sonja Christian, May Dang-Lawson, Caitlin Pritchard, Spencer A. Freeman, and Michael R. Gold. The Rap1-cofilin-1 pathway coordinates actin reorganization and MTOC
610 polarization at the B cell immune synapse. *Journal of Cell Science*, 130(6):1094–1109, 2017. ISSN 14779137. doi: 10.1242/jcs.191858.
- 611 46. Mukund Gupta, Bibhu Ranjan Sarangi, Joran Deschamps, Yasaman Nematbakhsh, Andrew Callan-Jones, Felix Margadant, René-Marc Mège, Chwee Teck Lim, Raphaël Voituriez, and Benoît
612 Ladoux. Adaptive rheology and ordering of cell cytoskeleton govern matrix rigidity sensing. *Nature communications*, 6(May):7525, 2015. ISSN 2041-1723. doi: 10.1038/ncomms8525.
- 613 47. D. Mitrossilis, J. Fouchard, D. Pereira, F. Postic, A. Richert, M. Saint-Jean, and A. Asnacios. Real-time single-cell response to stiffness. *Proceedings of the National Academy of Sciences of the
614 United States of America*, 107(38):16518–16523, 2010. ISSN 10916490. doi: 10.1073/pnas.1007940107.
- 615 48. J. Husson, K. Chemin, A. Bohineust, C. Hiroz, and N. Henry. Force generation upon T cell receptor engagement. *PLoS ONE*, 6(5), 2011. ISSN 19326203. doi: 10.1371/journal.pone.0019680.
- 616 49. King Lam Hui and Arpita Upadhyaya. Dynamic microtubules regulate cellular contractility during T-cell activation. *Proceedings of the National Academy of Sciences of the United States of America*,
617 114(21):E4175–E4183, 2017. ISSN 1091-6490. doi: 10.1073/pnas.1614291114.
- 618 50. Sara V. Merino-Cortés, Sofia R. Gardeta, Sara Roman-Garcia, Ana Martínez-Riaño, Judith Pineau, Rosa Liebana, Isabel Merida, Ana Maria Lennon Dumenil, Paolo Pierobon, Julien Husson,
619 Balbino Alarcon, and Yolanda R. Carrasco. Diacylglycerol kinase ζ promotes actin cytoskeleton remodeling and mechanical forces at the B cell immune synapse. *Science Signaling*, 13(627), apr
620 2020. ISSN 19379145. doi: 10.1126/scisignal.aaw8214.
- 621 51. Pieta K Mattila, Christoph Feest, David Depoil, Bebhinn Treanor, Beatriz Montaner, Kevin L Otipoby, Robert Carter, Louis B Justement, Andreas Bruckbauer, and Facundo D Batista. The Actin and
622 Tetraspanin Networks Organize Receptor Nanoclusters to Regulate B Cell Receptor-Mediated Signaling. *Immunity*, 38(3):461–474, mar 2013. ISSN 1097-4180. doi: 10.1016/j.immuni.2012.11.019.
- 623 52. B. Treanor, D. Depoil, A. Bruckbauer, and F. D. Batista. Dynamic cortical actin remodeling by ERM proteins controls BCR microcluster organization and integrity. *Journal of Experimental Medicine*,
624 208(5):1055–1068, 2011. ISSN 00221007. doi: 10.1084/jem.20101125.
- 625 53. C. Guedj, N. Abraham, D. Jullié, and C. Randriamampita. T cell adhesion triggers an early signaling pole distal to the immune synapse. *Journal of Cell Science*, 129(13):2526–2537, 2016. ISSN
626 14779137. doi: 10.1242/jcs.182311.
- 627 54. Jason Yi, Xufeng Wu, Andrew H. Chung, James K. Chen, Tarun M. Kapoor, and John A. Hammer III. Centrosome repositioning in T cells is biphasic and driven by microtubule end-on capture-
628 shrinkage. *Journal of Cell Biology*, 202(5):779–792, 2013. ISSN 00219525. doi: 10.1083/jcb.201301004.
- 629 55. N. Bourouina, J. Husson, F. Waharte, R. B. Pansu, and N. Henry. Formation of specific receptor-ligand bonds between liquid interfaces. *Soft Matter*, 7(19):9130–9139, 2011. ISSN 1744683X. doi:
630 10.1039/c1sm05659j.
- 631 56. R. Basu and M. Huse. Mechanical Communication at the Immunological Synapse. *Trends in Cell Biology*, 27(4):241–254, 2017. ISSN 18793088. doi: 10.1016/j.tcb.2016.10.005.
- 632 57. R. Wang, S. Zheng, and Y. George Zheng. *Polymer Matrix Composites and Technology*. Woodhead Publishing, 1st edition, 2011. ISBN 978-0-85709-221-2, 978-0-85709-222-9.
- 633 58. D. Vorselen, Y. Wang, M. M. de Jesus, P. K. Shah, M. J. Footer, M. Huse, W. Cai, and J. A. Theriot. Microparticle traction force microscopy reveals subcellular force exertion patterns in immune
634 cell–target interactions. *Nature Communications*, 11(1), 2020. ISSN 20411723. doi: 10.1038/s41467-019-13804-z.
- 635 59. T. G. Mason and J. Bibette. Shear rupturing of droplets in complex fluids. *Langmuir*, 13(17):4600–4613, 1997. ISSN 07437463. doi: 10.1021/la9700580.
- 636 60. N. Desprat, A. Guiry, and A. Asnacios. Microplates-based rheometer for a single living cell. *Review of Scientific Instruments*, 77:1–9, 2006.
- 637 61. Frédéric Pincet, Vladimir Adrien, Rong Yang, Jérôme Delacotte, James E. Rothman, Wladimir Urbach, and David Tareste. FRAP to Characterize Molecular Diffusion and Interaction in Various
638 Membrane Environments. *PLOS ONE*, 11(7):e0158457, jul 2016. ISSN 1932-6203. doi: 10.1371/JOURNAL.PONE.0158457.
- 639 62. Johannes Schindelin, Ignacio Arganda-Carreras, Erwin Frise, Verena Kaynig, Mark Longair, Tobias Pietzsch, Stephan Preibisch, Curtis Rueden, Stephan Saalfeld, Benjamin Schmid, Jean Yves
640 Tinevez, Daniel James White, Volker Hartenstein, Kevin Eliceiri, Pavel Tomancak, and Albert Cardona. Fiji: An open-source platform for biological-image analysis. *Nature Methods*, 9(7):676–682,
641 2012. ISSN 15487091. doi: 10.1038/nmeth.2019.
- 642 63. O. Mesdjian, N. Ruyssen, M. C. Jullien, R. Allena, and J. Fattaccioli. Enhancing the capture efficiency and homogeneity of single-layer flow-through trapping microfluidic devices using oblique
643 hydrodynamic streams. *Microfluidics and Nanofluidics* 2021 25:11, 25(11):1–10, oct 2021. ISSN 1613-4990. doi: 10.1007/S10404-021-02492-1.
- 644 64. Donald Wlodkowic, Shannon Faley, Michele Zagnoni, John P. Wikswo, and Jonathan M. Cooper. Microfluidic Single Cell Array Cytometry for the Analysis of Tumour Apoptosis. *Analytical Chemistry*,
645 81(13), 2009. ISSN 15378276. doi: 10.1021/ac9008463.Microfluidic.
- 646 65. Daniel S. Banks and Cécile Fradin. Anomalous diffusion of proteins due to molecular crowding. *Biophysical journal*, 89(5):2960–2971, 2005. ISSN 0006-3495. doi: 10.1529/BIOPHYSJ.104.051078.
- 647 66. T. C. Werner, J. R. Bunting, and R. E. Cathou. The shape of immunoglobulin G molecules in solution. *Proceedings of the National Academy of Sciences of the United States of America*, 69(4):
648 795–799, 1972. ISSN 00278424. doi: 10.1073/pnas.69.4.795.
- 649 67. P. Durand-Smet, E. Gauquelin, N. Chastrette, A. Boudaoud, and A. Asnacios. Estimation of turgor pressure through comparison between single plant cell and pressurized shell mechanics. *Physical
650 Biology*, 14(5), 2017. ISSN 14783975. doi: 10.1088/1478-3975/aa7f30.
- 651 68. Ben Fabry, Geoffrey N. Maksym, James P. Butler, Michael Glogauer, Daniel Navajas, and Jeffrey J. Fredberg. Scaling the microrheology of living cells. *Physical Review Letters*, 87(14):1–4, 2001.
652 ISSN 00319007. doi: 10.1103/PhysRevLett.87.148102.
- 653 69. M. Baland, N. Desprat, D. Icard, S. Féréol, A. Asnacios, J. Browaeys, S. Hénon, and F. Gallet. Power laws in microrheology experiments on living cells: Comparative analysis and modeling. *Physical
654 Review E - Statistical, Nonlinear, and Soft Matter Physics*, 74(2), 2006. ISSN 15502376. doi: 10.1103/PhysRevE.74.021911.
- 655 70. Anna Labernadie, Anaïs Bouissou, Patrick Delobelle, Stéphanie Balor, Raphael Voituriez, Amsha Proag, Isabelle Fourquaux, Christophe Thibault, Christophe Vieu, Renaud Poincloux, Guil-
656 laume M. Charrière, and Isabelle Maridonneau-Parini. Protrusion force microscopy reveals oscillatory force generation and mechanosensing activity of human macrophage podosomes. *Nature
657 Communications*, 5, 2014. ISSN 20411723. doi: 10.1038/ncomms6343.

658 71. Kalthoum Ben M'Barek. *Adhésion et phagocytose de gouttes d'émulsions fonctionnalisées*. PhD thesis, Université Pierre et Marie Curie, 2015.

Supplementary Information

Phenotyping Polarization Dynamics Of Immune Cells Using A Lipid Droplet - Cell Pairing Microfluidic Platform

Léa Pinon^{1,2,3}, Nicolas Ruysen⁴, Judith Pineau², Olivier Mesdjian^{1,3}, Damien Cuvelier^{3,5,11}, Anna Chipont⁶, Rachele Allena^{4,8}, Coralie L. Guerin^{6,7}, Sophie Asnacios^{9,10}, Atef Asnacios⁹, Paolo Pierobon^{2,✉}, and Jacques Fattaccioni^{1,3,✉}

¹École Normale Supérieure, UMR 8640, Laboratoire P.A.S.T.E.U.R., Département de Chimie, PSL Research University, Sorbonne Université, CNRS, 75005 Paris, France

²Institut Curie, U932, Immunology and Cancer, INSERM, 75005 Paris, France

³Institut Pierre-Gilles de Gennes pour la Microfluidique, 75005 Paris, France

⁴Arts et Métiers Institute of Technology, Université Paris 13, Sorbonne Paris Cité, IBHGC, HESAM Université, F-75013 Paris, France

⁵Institut Curie, UMR 144, PSL Research University, CNRS, Paris, France

⁶Institut Curie, Cytometry Platform, F-75005, Paris, France.

⁷Université Paris Cité, INSERM, Innovative Therapies in Haemostasis, F-75006, Paris, France.

⁸LJAD, UMR 7351, Université Côte d'Azur, 06100, Nice, France

⁹Université de Paris, CNRS, Laboratoire Matière et Systèmes Complexes, UMR 7057, F-75013, Paris, France

¹⁰Sorbonne Université, Faculté des Sciences et Ingénierie, UFR 925 Physics, F-75005 Paris, France

¹¹Sorbonne Université, Faculté des Sciences et Ingénierie, UFR 926 Chemistry, F-75005 Paris, France

Supplementary Note 1: Microfluidic Chip Computational Fluid Dynamics Characterization

The 15 μm -thick U-traps can immobilize 12 μm -large droplets and B lymphocytes (IIA1.6 cell lines) of comparable size.

The traps are 10 μm -thick traps and are raised by 5 μm -thick pillars to ensure a continuous flow into the chip (**Fig. 3C**).

Thanks to the pillars, the fluid streamlines are not deviated when a first object is trapped in the weir structures, hence they allow the easy capture of a second object such as a B lymphocyte.

We sought to determine the inlet pressure to impose into the chamber to mimic a shear stress in the same order of magnitude of 0.6 Pa, representing the wall shear stress close to the afferent vessel (29). We first modeled the fluid flow into the entire designed microfluidic chamber with a 2D depth averaged Computational Fluid Dynamic (CFD) model according to inlet pressures from 0 to 1000 Pa. We deduced the corresponding pressure gap occurring around each trap thanks to isobar lines (**Fig. 1D** and **1E**). From these pressure gap values we built a 3D CFD model of the flow inside and around a U-trap occupied by a droplet and a B-cell that we considered as rigid bodies. This approach is very similar to the one proposed in (64). From the fluid velocity field, we calculated the fluid shear rate and deduced the fluid shear stress norm applied on the B cell (considering the fluid as Newtonian). Particular attention was paid to ensure mesh convergence of the results using boundary layer elements and mesh refinement on the B-cell boundaries. We obtained a maximal shear stress on B cell between 0.07 and 0.75 Pa (lower blue dashed and pointed curve in **Fig. S3 C-D**) for the least loaded trap and between 0 and 1.0 Pa for the most loaded trap (above red dashed curve **Fig. S3 C-D**). These values suggest that shear stress occurring on the B cell in our device is totally comparable to the in-vivo shear stress experienced by B cells in lymph nodes.

Supplementary Note 2: Titration of antigen concentration on droplet surface

We first titrate streptavidin attachment by measuring the adsorption isotherm onto the phospholipid-coated droplet surface (see **Materials and Methods** section for details). The bulk concentration of streptavidin is expressed in molar equivalents,

696 i.e. the theoretical amount of proteins necessary to cover the droplet sample with a close packed monolayer as described
697 in (33). For instance, one equivalent of streptavidin for 10 million of 11 μm -large droplets corresponds to $4 \cdot 10^{-10}$ moles
698 of proteins (**Table S3**). The fluorescence of the droplets is characterized by epifluorescence microscopy, following the
699 method detailed in Pinon *et al.* (33). The streptavidin adsorption isotherm fits with a Langmuir isotherm with a K_{Strep} ,
700 the streptavidin concentration producing half occupation, equal to $9.7 \pm 4.7 \text{ eq}^{-1}$ compatible with our previous analyses
701 (**Figure 1D**) (33).

702 For a bulk concentration of streptavidin corresponding to a maximal surface coverage (1 eq.), we measured the adsorption
703 isotherm of antigens (F(ab')_2) using fluorescent secondary antibodies and epifluorescence microscopy for the quantitative
704 fluorescence measurements of the total amount of proteins attached to droplets. **Figure 1E** shows that the antigen
705 adsorption isotherm fits with a Langmuir isotherm with a $K_{Ag} = 1.74 \pm 0.74 \text{ eq}^{-1}$. We finally converted the streptavidin
706 fluorescence intensity value in a molecular equivalent of proteins using fluorescence calibration beads, and knowing the
707 average number of dyes attached per streptavidin (and therefore per F(ab')_2 , **Supplementary Note 2**).

708

709 The fitting curves of titrations used in **Fig. 2** follow Langmuir isotherms, hence the fluorescence intensity varies in time as

710

$$I(C) = I_{Max} \frac{KC}{1 + KC} \quad (\text{S1})$$

711 where C is the bulk concentration of the molecule of interest, K the affinity constant and I_{Max} the fluorescence intensity
712 at large C .

713 Molecules of equivalent soluble fluorophore (MESF) is converted to antigen surface concentration as follows:

$$\rho_{Ag} = N_{Ag}/S_{droplet} = \frac{\text{MESF}}{N_f \frac{S_{Strep}}{S_{Ag}} \cdot S_{droplet}} \quad (\text{S2})$$

714 where S_{Strep} and S_{Ag} , are the respective geometric area of a streptavidin molecule (65) and of a F(ab')_2 fragment (66),
715 $S_{droplet}$ is the droplet surface, and N_f is the number of fluorophores per streptavidin (as streptavidin is tetravalent, and
716 one bond is occupied by the lipid biotin, we considered $N_f=3$).

717 **Supplementary Note 3: Elastic and viscous moduli of oil droplets**

718 Elastic-like behavior is characterized by proportionality between the stress σ and strain ϵ , typically $\sigma_e = E\epsilon$, with E the
719 elastic modulus characteristic of the material. Viscous response is characterized by proportionality between the stress σ
720 and strain rate $\frac{d\epsilon}{dt}$, typically $\sigma_v = \eta \cdot \frac{d\epsilon}{dt}$, with η the viscosity of the material. When elastic and viscous stresses add up, and
721 using complex notation to describe dynamic rheology (oscillating stress and strain at $\omega = 2\pi f$, where f is the frequency),
722 one gets:

$$\sigma^* = (E + i\eta\omega)\epsilon^* \quad (\text{S3})$$

723 The complex viscoelastic modulus G^* is defined as:

$$G^* = \sigma^* / \epsilon^* = G' + iG'' \quad (\text{S4})$$

724 Thus, one finds, for the so called Kelvin-Voigt viscoelastic model:

$$G' = E \quad (\text{S5})$$

725 and

$$G'' = \eta\omega \quad (\text{S6})$$

726 Let us now consider an oil droplet of resting diameter L_0 , characterized by a surface tension γ and a shear viscosity
727 η . When uniaxially compressed between parallel microplates, it develops a restoring (elastic-like) force due to Laplace
728 pressure $\Delta P = 4\gamma/L_0$ and a viscous dissipative drag proportional to the elongational viscosity, $\eta_e = 3\eta$ for a newtonian
729 liquid.

730 When the droplet is compressed from its resting diameter L_0 to a slightly smaller size L , using a Hertz-like model for
731 a small indentation $(L_0 - L)/2$, one finds that the static force resisting compression is simply $F_e = \Delta P \pi L_0 (L_0 - L)/4$,
732 where $\pi L_0 (L_0 - L)/4$ is the droplet-microplate contact area and ΔP the Laplace excess pressure. Thus, the elastic-like
733 stress is simply ΔP , and the storage modulus $G' = \Delta P/\epsilon$ (67), where $\epsilon = (L_0 - L)/L_0$ is the droplet strain. Expressing
734 the modulus as function of the surface tension, one finds $G' = 4\gamma/\epsilon L_0$, hence the fitting curve used in **Fig. 2D** to estimate
735 the surface tension of the droplets. Indeed, setting $\epsilon_0 = 0.2$ as in our experiments, with typically $L_0 = 20 \mu\text{m}$ and $\gamma = 1$
736 mN/m, one finds $G' = 1000 \text{ Pa}$ as typically measured with the microplates setup.

737

738 The viscous contribution to the complex modulus can be estimated from the drag force $F_v \sim 3\pi\eta V L_0$. Using the Hertz-like
739 estimation of the droplet-microplate contact area, the stress is expressed as:

$$\sigma = \frac{F_v}{\pi L_0 (L_0 - L)/4} \sim \frac{12\eta V}{(L_0 - L)} \quad (\text{S7})$$

740 Expressing the typical speed V as function of the rate of strain $V = L_0(d\epsilon/dt)$, one gets:

$$\sigma \sim \frac{12\eta}{\epsilon} \cdot \frac{d\epsilon}{dt} \quad (\text{S8})$$

741 Using the equation **S4**, one finds:

$$G'' \sim \frac{12\eta\omega}{\epsilon} = \frac{24\pi\eta f}{\epsilon} \quad (\text{S9})$$

742 For $f = 1 \text{ Hz}$, $\epsilon_0 = 0.2$ and the lipiodol viscosity at 37°C $\eta = 0.025 \text{ Pa}\cdot\text{s}$, one finds $G'' (1 \text{ Hz}) = 10 \text{ Pa}$ which is the right

743 order of magnitude (**Fig. 2G**).

744 As a consequence, comparing $G' = 1000$ Pa and $G'' = 10$ Pa, we consider that the viscous contribution can be neglected
745 for processes taking place over time scales longer than a second, and we only take into account the storage modulus
746 over the loss one: $G^*(f) \sim G'$. Since G' is constant over the explored frequency range (**Fig. 2G**), $G^*(f) \sim G'$ is thus
747 considered as an apparent Young modulus.

748 **Supplementary Note 4: Characterization of B cell mechanics**

749 B cell viscoelastic properties was assessed by microplate microrheology. Experiment on single cells show that B cell
750 mechanical properties follow a damping model (**Fig. 2F**). G' and G'' mainly behave as weak power laws of the frequency
751 (68, 69) (**Fig. 2F**) with a power law exponent similar to those already reported for immune cells ($\alpha \approx 0.16$), and exhibit an
752 apparent visco-elastic modulus of about 165 Pa (**Fig. 2G**).

753 **Supplementary Note 5: Characterization of antigen mobility on droplets**

754 An interesting difference between two types of functionalization (bulk vs. surface) is that the B cell is able to gather the
755 antigen only in the first case, despite polarizing correctly in both cases. One possible cause could be a difference in the
756 antigen mobility. We quantified the mobility of the antigen in the two types of droplet by measuring the diffusion coefficient
757 by Fluorescence Recovery After Photobleaching (FRAP) following the protocol described in (61). Diffusion coefficients
758 of bulk- and surface-functionalized droplets are respectively equal to $0.13 \pm 0.09 \mu\text{m}^2/\text{s}$ (N=12) and $0.05 \pm 0.03 \mu\text{m}^2/\text{s}$
759 (N=12): the two values are significantly different (**Fig. S7**).

760
761 Of note, cells known to exert stronger forces, such as macrophages (70), are able to form a cluster of antigens on both
762 types of droplets (24) meaning independently of functionalization process, confirming that the antigen cluster is driven by
763 cell forces. Further molecular dynamic simulations or FRAP experiments out of equilibrium are required to elucidate the
764 physical mechanisms linking pulling forces and active antigen accumulation.

765 **Supplementary Figures**

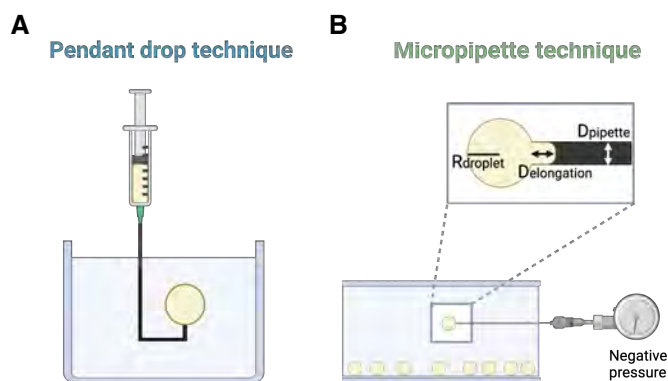


Fig. S1. Schematics of pendant drop and micropipette aspiration techniques. (A) The pendant drop technique consists in measuring the interfacial tension of an oil drop in an aqueous phase (water and surfactants). A dedicated software tracks the drop shape and, depending on oil and aqueous phase properties (type and concentration of surfactants and viscosity), computes the interfacial tension over time. (B) Interfacial tension of stabilized droplets is determined by applying a negative pressure on droplets via a micropipette. The interfacial tension γ is computed from the negative pressure required to aspire a droplet until forming an elongation whose dimension is equal to the micropipette size, as $\gamma = \Delta P R_p / 2$.

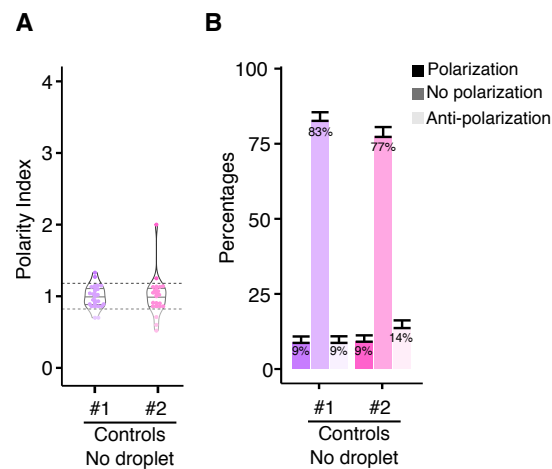


Fig. S2. Control of polarization without droplets. Polarity index (left) and percentages of polarized, non polarized and anti-polarized cells (right) without being in contact with droplets. Control #1 has been realized without droplets in the whole chip (N=23 cells, n=3 independent experiments) while control #2 has been realized on non-interacting cells located nearby trapped droplets (N=22, n=3). In both cases, polarization percentage is similar to BSA-coated droplets results.

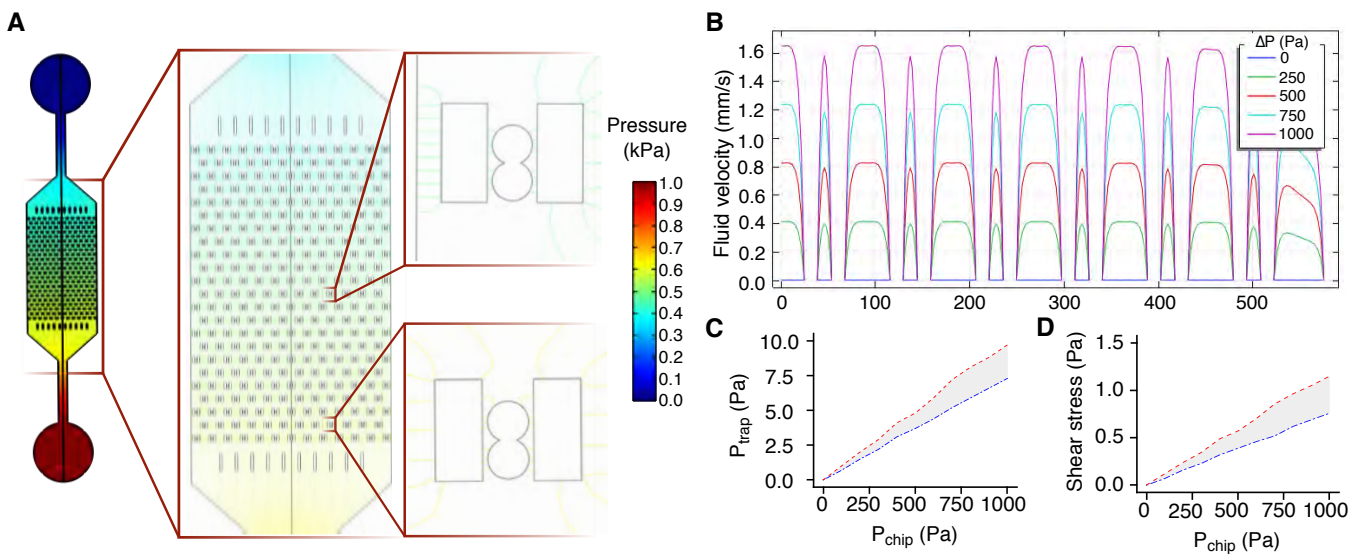


Fig. S3. Microfluidic Chip Computational Fluid Dynamics Characterization. (A) Pressure field in the microfluidic chamber for a pressure drop between inlet and outlet about 1 kPa. Each isobar line represents a 1 Pa-step. Depending on trap locations, the pressure variation before and after the trap is between 7.3 and 9.7 Pa. (B) Fluid velocity profiles on a middle cut line depending on the pressure applied at the chip entrance without considering trapped objects, ranging between 0 and 1000 Pa. (C) Pressure drop in a trap depending on the pressure applied in the chip. (D) Shear stress on a trapped cell assumed as rigid, depending on the pressure applied in the chip. (C)-(D) The red curves are obtained for the most mechanically loaded traps, and the blue curves for the least mechanically loaded ones. Simulations were performed with Comsol.

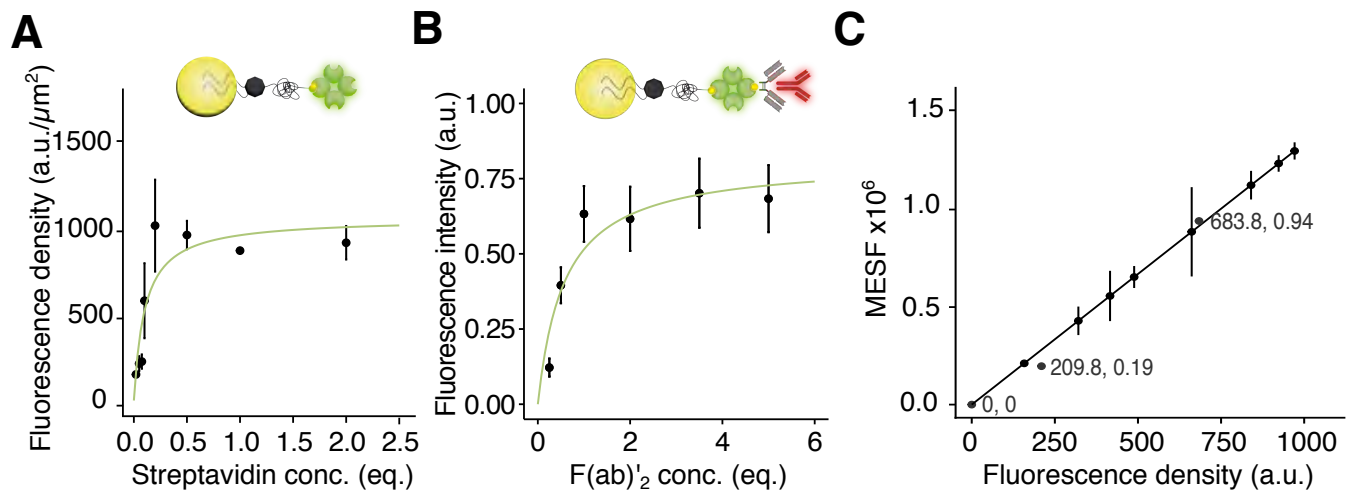


Fig. S4. Titration of antigen concentration on droplet surface. (A) Experimental titration curve of streptavidin molecules on 11 μm -large droplets, initially coated with 100 equivalents of DSPE-PEG₂₀₀₀-biotin. (B) Experimental titration curve of F(ab')₂ fragments on 11 μm large droplets, initially functionalized with 100 equivalents of DSPE-PEG₂₀₀₀-biotin and 1 equivalent of Streptavidin. Non-fluorescent F(ab')₂ fragments are imaged with a secondary fluorescent anti-F(ab')₂ antibody, with a 1:1 ratio. (C) Calibration curve of commercial FITC fluorescent Quantum™ MESF (Bang Laboratories, Inc.) and streptavidin-coated droplets. Fluorescence intensity of beads and droplets have been measured by microscopy (channel GFP). Fluorescence intensity of Quantum™ MESF (dark gray dots) are correlated to MESF provided by the company (coordinates are indicated). MESF of droplets have been determined thanks to the linear function $y = 1374.67x$.

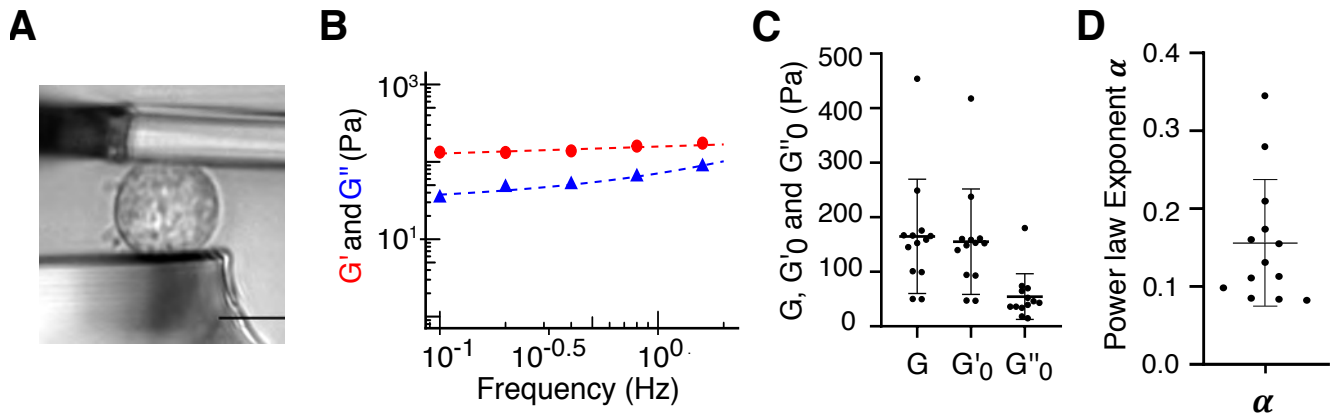


Fig. S5. Characterization of B cell mechanics. (A) Representative brightfield image of a B cell immobilized between the microplates. Scale bar: 10 μm . (B) Elastic G' and viscous G'' modulus of a single B cell plotted as a function of the probing frequency. Both G' and G'' follow a power law. (C) Summary graph of the G' , G'' and G^* values of the B cells probed by microplates (N=13 cells, n=3 independent experiments). The average values of G'_0 , G'_0 and G''_0 are respectively equal to 165.0 ± 57.0 Pa, 155.4 ± 52.54 Pa, and 54.5 ± 22.7 Pa. (D) For B cells, the complex modulus G follows a power law of the frequency with coefficient α : $G' = G'_0 f^\alpha$ and $G'' = G''_0 f^\alpha$. The exponent is determined from fitting of both moduli: $\alpha = 0.155 \pm 0.04$ (N=13, n=3 independent experiments), corresponding to values measured for immune cells.

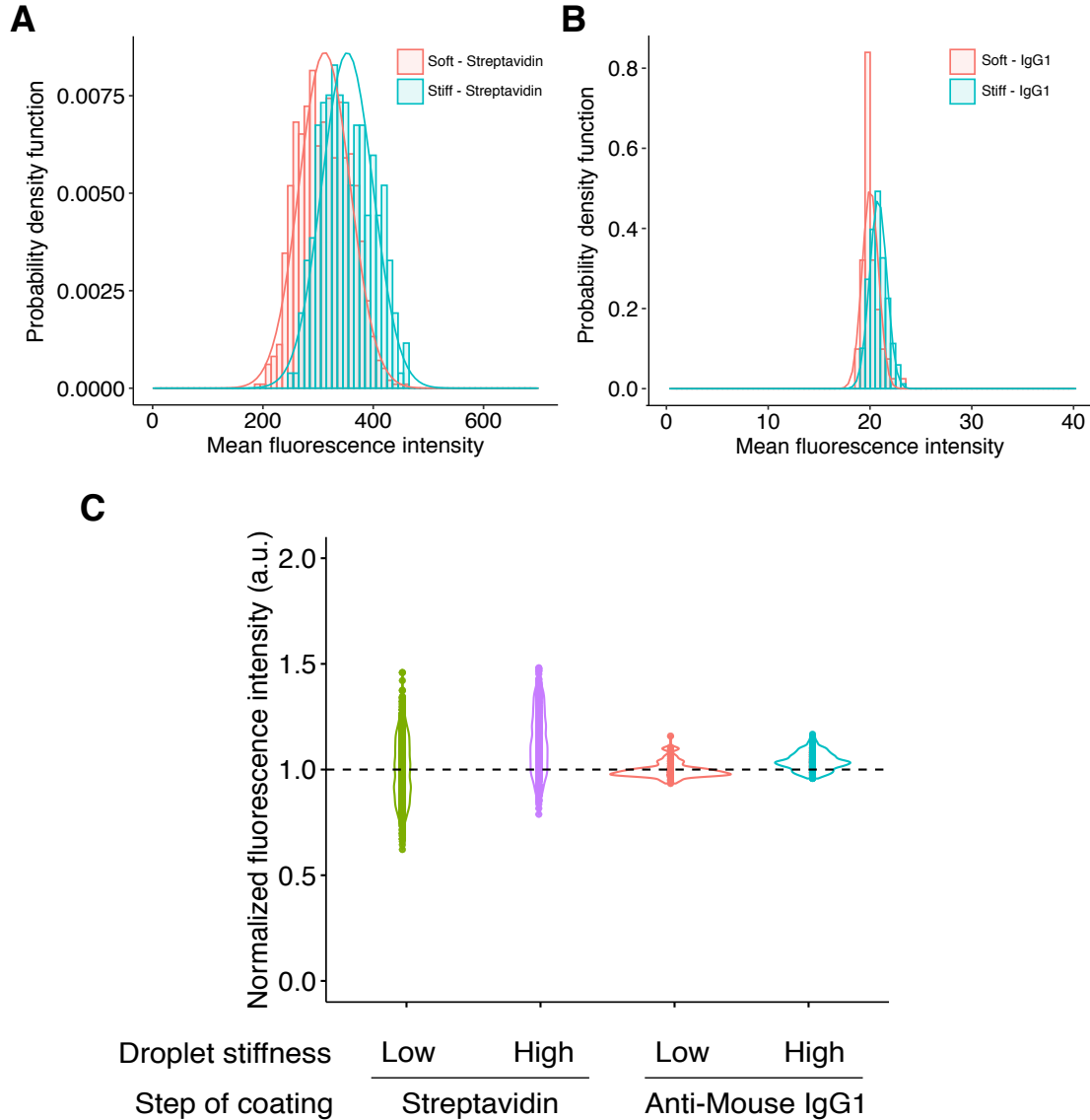


Fig. S6. Antigen coating depending on droplet stiffness. Fluorescence intensities of 0.5 equivalent Anti-mouse IgG1 κ Isotype (Alexa Fluor 647) (A) on 1 equivalent of streptavidin (Alexa Fluor 488) (B) coated by soft and stiff droplets. Each histogram is fitted with a gaussian curve with mean \pm sd (% sd/mean): values are 19.79 ± 0.79 (4%) (stiffness^{low}, IgG1), 20.54 ± 0.84 (4%) (stiffness^{high}, IgG1), 312 ± 46 (15%) (stiffness^{low}, streptavidin), 353 ± 46 (14%) (stiffness^{high}, streptavidin). (C) Pooled graph of normalized fluorescence intensities. Intensities relative to stiff droplets are normalized by the mean value of soft droplets for both conditions, IgG1 and Streptavidin.

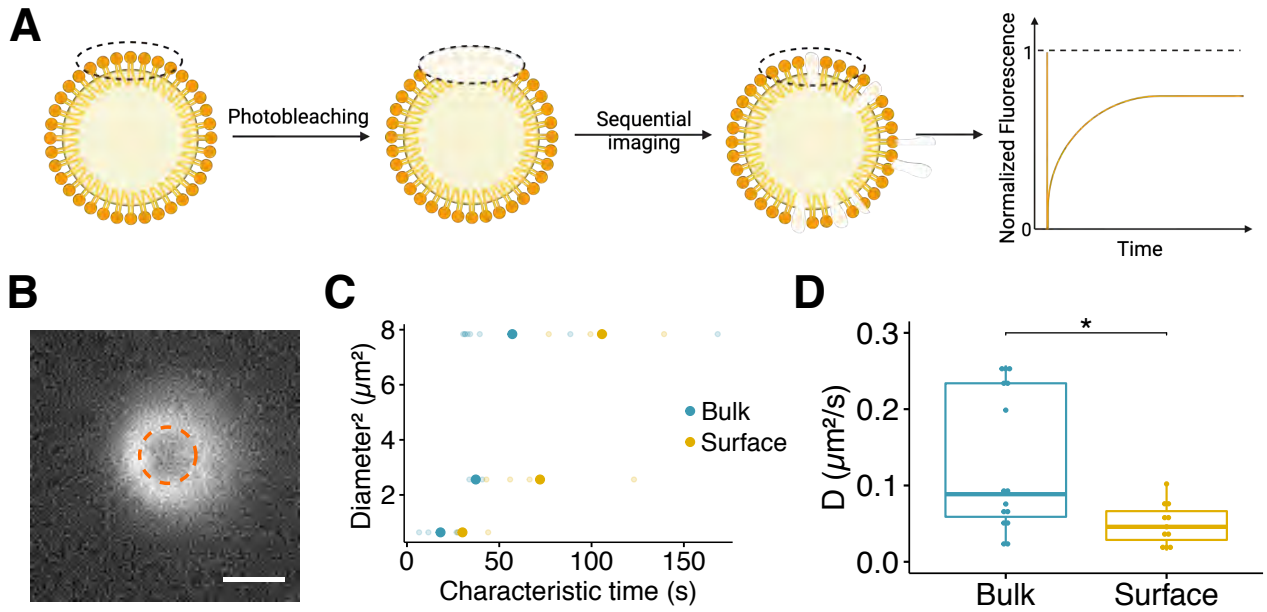


Fig. S7. FRAP Experiments - Antigen diffusion. (A) Scheme of the experimental setup. A circular area on top of a single antigen-coated droplet is bleached. The fluorescence recovery is recorded over 5 min and finally plotted to deduce the diffusion coefficient. (B) Confocal image of a bleached functionalized droplet. The bleached area is surrounded by a dashed circle. Scale bar: 5 μm . (C) Correlation of the bleached area and the relative characteristic time for bulk- and surface-functionalized droplets. The shaded dots represent the individual values and the main solid points the mean value. (D) Diffusion coefficients of bulk- and surface-functionalized droplets determined via FRAP experiments, are respectively equal to $0.13 \pm 0.09 \mu\text{m}^2/\text{s}$ (N=15 droplets) and $0.05 \pm 0.03 \mu\text{m}^2/\text{s}$ (N=11 droplets). * indicates p-value < 0.05, Wilcoxon test.

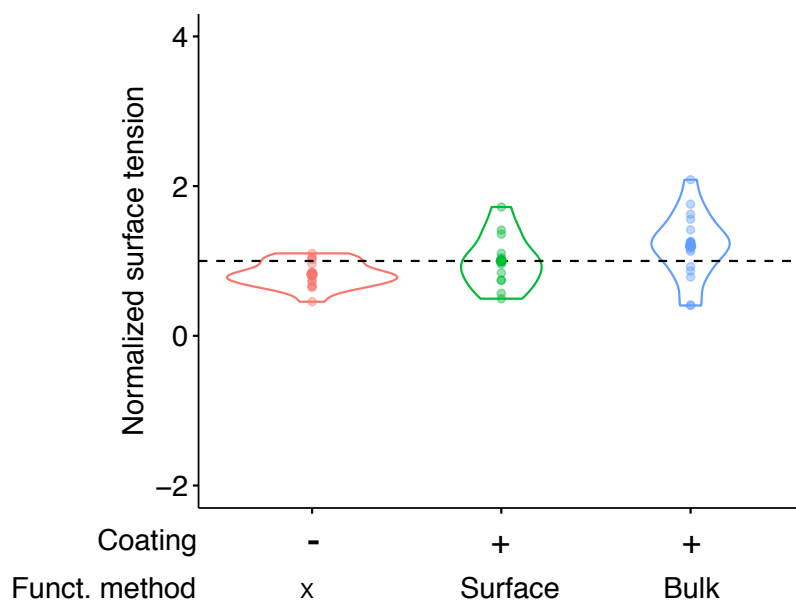


Fig. S8. Surface tensions dependence upon functionalization method. Surface tension micropipette measurements of non-coated soybean oil droplets, surface-functionalized and bulk-functionalized $F(ab')_2$ -coated soybean oil droplets. Values are normalized by the mean surface tension obtained for the surface-functionalized droplets for sake of clarity. Differences in surface tensions between different coatings and functionalization methods are not significant.

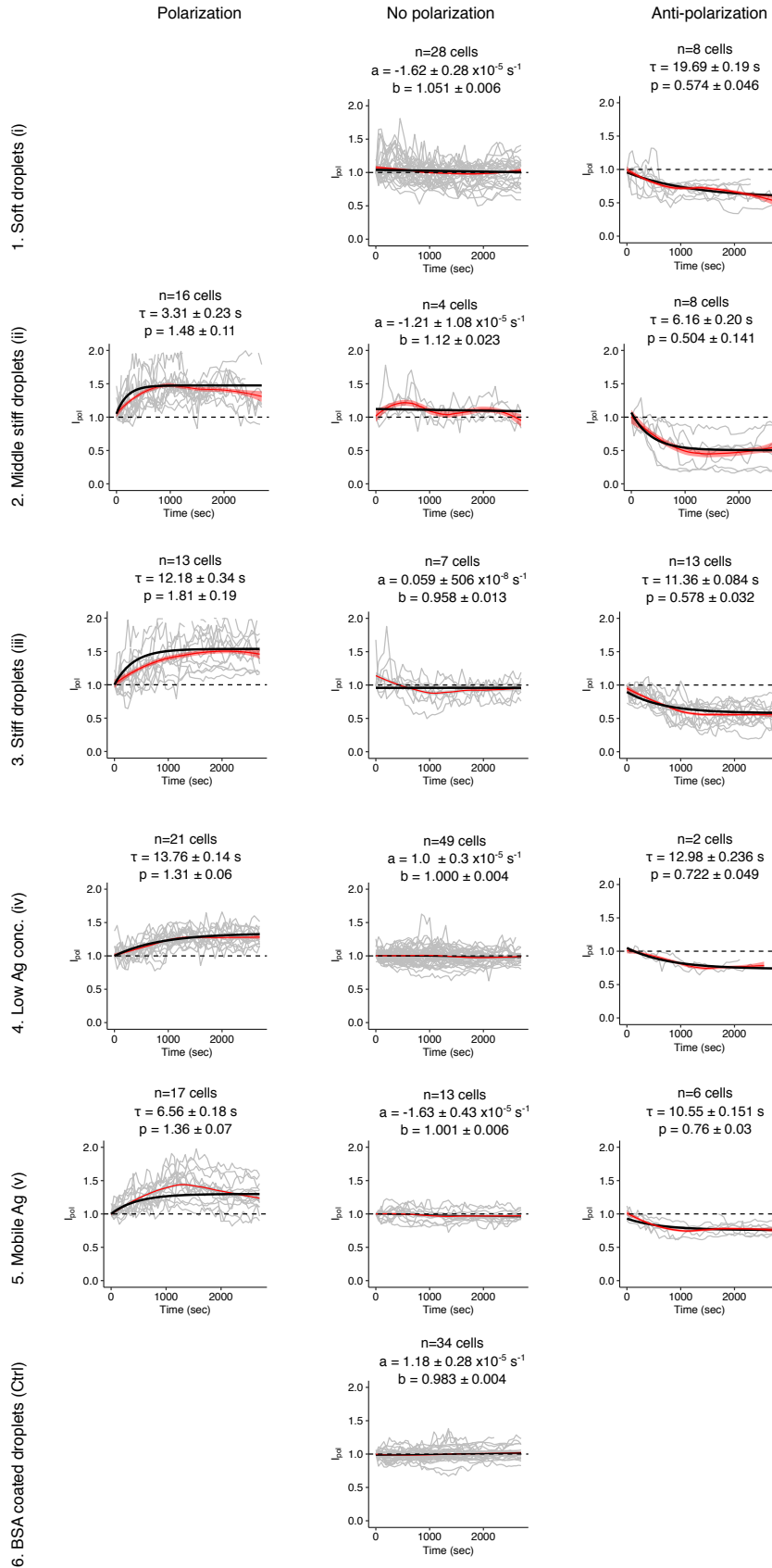


Fig. S9. Cellular phenotype of B lymphocytes dynamics. The exponential polarization and anti-polarization fits follow respectively $y_{pol} = (p - 1)(1 - \exp(-t/\tau)) + 1$ and $y_{antipol} = (1 - p)(1 - \exp(-t/\tau)) + 1$, where τ is the characteristic time and p the related plateau. The non-polarized phenotype is characterized by a linear fit: $y_{nopol} = ax + b$.

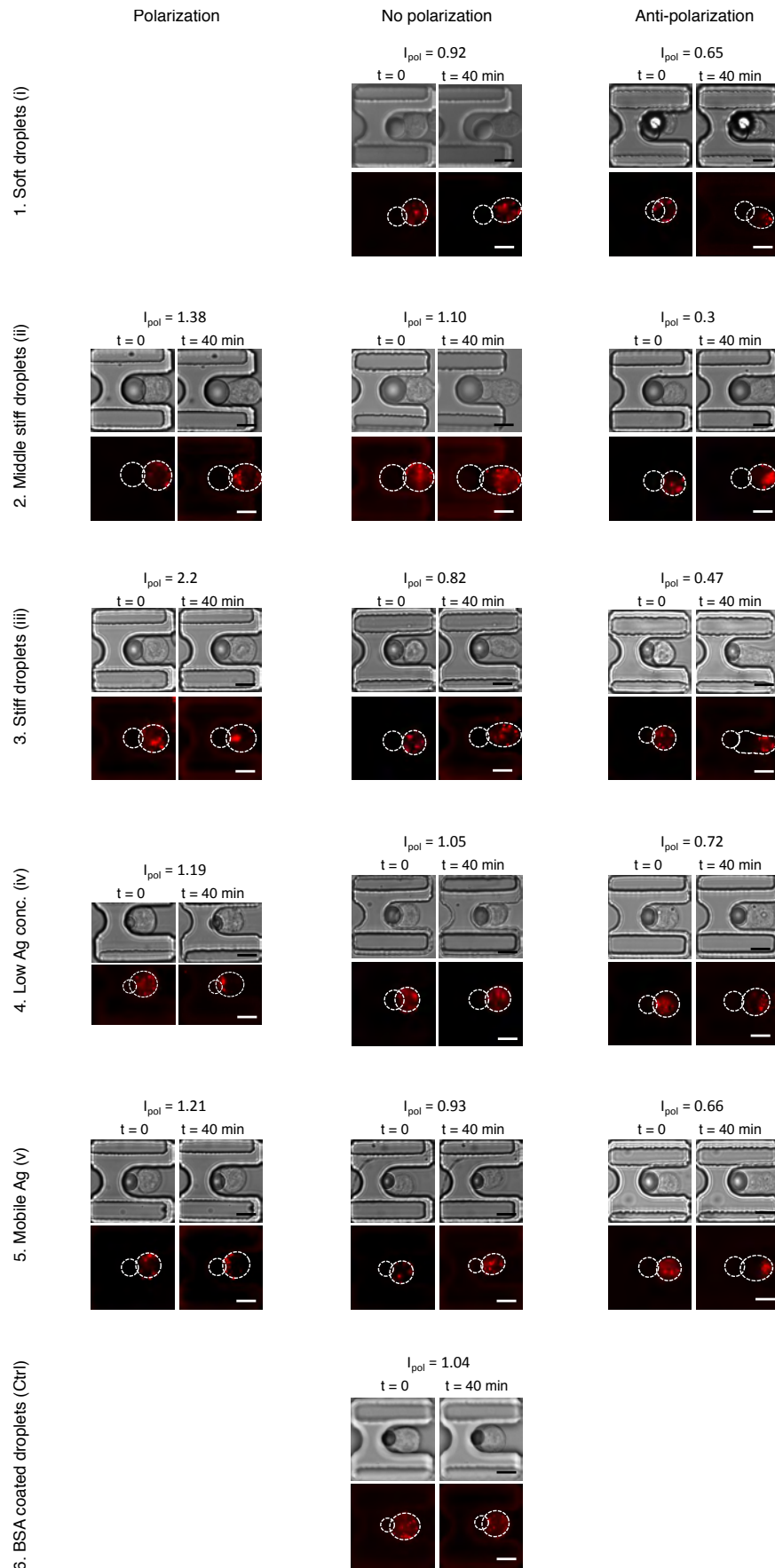


Fig. S10. Microscopy image of B lymphocytes dynamics. Images show the first time point (contact) and the final one (40 minutes) for different droplet conditions and for the three behaviors (polarization, no polarization, and anti-polarization). Scale bar: 10 μm .

766 **Supplementary Tables**

Oil phase	Water Phase	Surface tension (mN/m)
Mineral oil + Oleic acid 5%v/v	F68 15%	1.69 ± 0.19
Mineral oil	F68 15%	4.73 ± 0.38
Soybean oil	F68 15%	12.03 ± 0.52
Lipiodol oil	F68 15%	1.52 ± 0.12
Lipiodol oil + Oleic acid 5%v/v	F68 15%	0.88 ± 0.12

Table S1. Interfacial tension of oil/aqueous phases via pendant drop technique.

Oil phase	Functionalization	Surface tension \pm SD (mN/m)
Lipiodol oil + Oleic acid 5%v/v	None	2.36 ± 0.31
Lipiodol oil + Oleic acid 5%v/v	DSPE-PEG-Biotin	2.50 ± 0.24
Soybean oil	DSPE-PEG-Biotin	$10 \pm 2^*$

Table S2. Interfacial tension of oil/aqueous phases via micropipette technique. Measurements have been performed on droplets stabilized by Pluronic F68 and surrounded by an aqueous phase (Phosphaste buffer/Tween 20 at CMC). *From (71)

Functionalization	Equivalent	Conc.(mg/ml)	Volume (μL)
DSPE-PEG(2000)-Biotin	100	10	3.60
Streptavidin	1	1	5.43
Biotinylated F(ab') ₂	1	1.4	0.98
Secondary Antibody	1	0.8	2.35

Table S3. Table depicting the equivalent and the volume required to coat 2 millions of 12 μ m-large droplets, via surface functionalization method.

767 **Supplementary Movies**

768 Movie S1: Active recruitment of antigen at the B cell (IIA1.6) synapse in contact with a F(ab')₂-coated bulk-functionalized
769 stiff droplet. 40X objective, epifluorescence microscope, LysoTracker DND staining. Timeframe: 50 s.

770 Movie S2: Polarized B cell IIA1.6 in contact with a F(ab')₂-coated surface-functionalized stiff droplet. 40X objective,
771 epifluorescence microscope, LysoTracker DND staining. Timeframe: 50 s.

772 Movie S3: Anti-Polarized B cell IIA1.6 in contact with a F(ab')₂-coated surface-functionalized stiff droplet. 40X objective,
773 epifluorescence microscope, LysoTracker DND staining. Timeframe: 50 s.